

# The metal-insulator transitions of VO<sub>2</sub>: A band theoretical approach

Volker Eyert\*

Institut für Physik, Universität Augsburg, 86135 Augsburg, Germany

Received 9 July 2002, accepted 30 July 2002 by B. Kramer

**Abstract.** The results of first principles electronic structure calculations for the metallic rutile and the insulating monoclinic M<sub>1</sub> phase of vanadium dioxide are presented. In addition, the insulating M<sub>2</sub> phase is investigated for the first time. The density functional calculations allow for a consistent understanding of all three phases. In the rutile phase metallic conductivity is carried by metal  $t_{2g}$  orbitals, which fall into the one-dimensional  $d_{||}$  band, and the isotropically dispersing  $e_g^\pi$  bands. Hybridization of both types of bands is weak. In the M<sub>1</sub> phase splitting of the  $d_{||}$  band due to metal-metal dimerization and upshift of the  $e_g^\pi$  bands due to increased  $p$ - $d$  overlap lead to an effective separation of both types of bands. Despite incomplete opening of the optical band gap due to the shortcomings of the local density approximation, the metal-insulator transition can be understood as a Peierls-like instability of the  $d_{||}$  band in an embedding background of  $e_g^\pi$  electrons. In the M<sub>2</sub> phase, the metal-insulator transition arises as a combined embedded Peierls-like and antiferromagnetic instability. The results for VO<sub>2</sub> fit into the general scenario of an instability of the rutile-type transition-metal dioxides at the beginning of the  $d$  series towards dimerization or antiferromagnetic ordering within the characteristic metal chains. This scenario was successfully applied before to MoO<sub>2</sub> and NbO<sub>2</sub>. In the  $d^1$  compounds, the  $d_{||}$  and  $e_g^\pi$  bands can be completely separated, which leads to the observed metal-insulator transitions.

**Keywords:** transition-metal oxides, metal-insulator transition, electronic structure

**PACS:** 71.20.-b, 71.30.+h, 72.15.Nj

## 1 Introduction

At a temperature of 340 K and ambient pressure, stoichiometric VO<sub>2</sub> undergoes a metal-insulator transition, which is accompanied by a structural transition from a high-temperature rutile phase to a low-temperature monoclinic phase [1, 2]. Since its discovery more than forty years ago, this transition has been attracting considerable interest for fundamental reasons, and for possible applications [2]. The latter result from the abrupt change in the resistivity over several orders of magnitude, as well as from the fact that the transition occurs near room temperature [1, 2]. Despite this strong motivation, our understanding of the origin of the phase transition is still far from complete. Several models have been proposed ranging from Peierls- [3, 4, 5, 6, 7, 8, 9] to Mott-Hubbard-type [10, 11, 12, 13] scenarios. They stress, to a different degree, the role of lattice instabilities, electron-phonon interaction and

---

\*Corresponding author: eyert@physik.uni-augsburg.de

electron-electron correlations. So far, neither of these approaches has been successful in explaining the broad range of phenomena occurring in vanadium dioxide. In particular, a complete and generally accepted picture of the physics of this material has not yet been developed. More generally, a comprehensive understanding of the rutile-related transition-metal dioxides is not available.

This class of materials has been intensively studied for a long time, due to the complexity of the physical properties [14]. As is obvious from Tab. 1 this diversity

**Table 1** Properties of transition-metal dioxides with rutile-related structure (from Ref. [15]).

	$d^0$	$d^1$	$d^2$	$d^3$	$d^4$	$d^5$	$d^6$
<b>3d</b>	TiO <sub>2</sub> (S)	VO <sub>2</sub> <sup>*</sup> (M-S)	CrO <sub>2</sub> (F-M)	MnO <sub>2</sub> (AF-S)			
<b>4d</b>		NbO <sub>2</sub> <sup>*</sup> (M-S)	MoO <sub>2</sub> <sup>*</sup> (M)	TcO <sub>2</sub> <sup>*</sup> (M)	RuO <sub>2</sub> (M)	RhO <sub>2</sub> (M)	
<b>5d</b>		TaO <sub>2</sub> (?)	WO <sub>2</sub> <sup>*</sup> (M)	ReO <sub>2</sub> <sup>*</sup> (M)	OsO <sub>2</sub> (M)	IrO <sub>2</sub> (M)	PtO <sub>2</sub> <sup>*</sup> (M)

\* deviations from rutile, M = metal, S = semiconductor  
F/AF = ferro-/antiferromagnet

shows up mainly in the 3d series, which comprises, in addition to VO<sub>2</sub>, the large-gap semiconductor TiO<sub>2</sub>, the half-metallic ferromagnet CrO<sub>2</sub>, and the antiferromagnetic semiconductor MnO<sub>2</sub> [15, 16]. In contrast, except for NbO<sub>2</sub>, which, like VO<sub>2</sub>, undergoes a metal-insulator transition accompanied by a structural transition, the 4d and 5d compounds are neither semiconducting nor magnetic. Nevertheless, there exist several members in each group, which display small but characteristic deviations from the rutile structure [14, 15, 17].

Interestingly, the distortions of the rutile structure found at the phase transitions of VO<sub>2</sub> and NbO<sub>2</sub> are very similar for all the transition-metal dioxides which display such deviations, i.e. for VO<sub>2</sub>, NbO<sub>2</sub>, MoO<sub>2</sub>, WO<sub>2</sub>, TcO<sub>2</sub>, and  $\alpha$ -ReO<sub>2</sub> [14]. They are characterized by two distinct modes, namely a pairing of the metal atoms along characteristic chains parallel to the tetragonal  $c$  axis, and a lateral zigzag-like displacement [18, 14, 19, 20]. This leads to the so-called M<sub>1</sub> structure, which has a simple monoclinic lattice. The unit cell is twice as large as that of the rutile structure. NbO<sub>2</sub> is an exception: below the transition temperature this compound has a body-centered tetragonal lattice with a unit cell, which comprises 16 rutile cells [21]. Due to the strong metal-metal bonding within the chains parallel to the rutile  $c$  axis, which causes the aforementioned pairing, the above six dioxides have the smallest ratios of the symmetrized lattice constants  $c_R/a_R$  (Fig. 1).

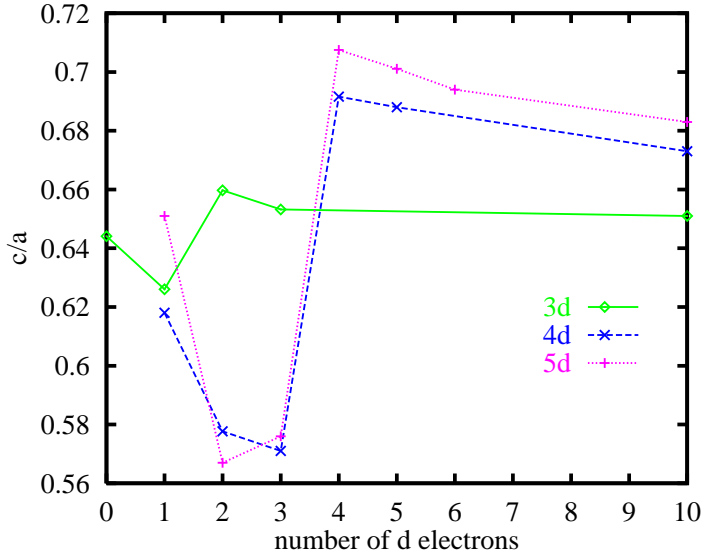


Fig. 1 Axial ratios of rutile-related transition-metal dioxides.

The structural similarities of the six compounds mentioned above are in contrast to their completely different electronic properties: while the  $d^1$  compounds VO<sub>2</sub> and NbO<sub>2</sub> undergo a metal-insulator transition, their four  $d^2$  and  $d^3$  neighbours like all other  $4d$  and  $5d$  compounds listed in Tab. 1 remain metallic at all temperatures. An explanation for this diversity is still lacking. The different trends in the structural and electronic properties within the transition-metal dioxides at the beginning of the  $d$  series led Goodenough to rule out the Jahn-Teller effect as a major source for the crystal structure characteristics [3]. Mechanisms based on Fermi surface nesting could be excluded due to the change in  $d$  electron occupation. A comprehensive theory, explaining both the structural similarities of all the above transition-metal dioxides and the diversity in their electronic properties on an equal footing, is still missing.

The discovery of two additional insulating low-temperature phases of VO<sub>2</sub> led to further complications. These phases, denoted T and M<sub>2</sub>, appear on doping or applying uniaxial pressure. They are generally regarded as metastable forms of stoichiometric VO<sub>2</sub> at ambient pressures. Their crystallographic distortions and magnetic properties add to the wealth of phenomena observed in vanadium dioxide, and demonstrate even more our lack in understanding.

We have studied the transition-metal dioxides at the beginning of the  $d$  series using density functional theory based electronic structure calculations [22]. In particular, our investigations so far include metallic MoO<sub>2</sub> as well as the other metal-insulator transition system besides VO<sub>2</sub>, namely NbO<sub>2</sub> [23, 24]. In the present paper we report on results of the different phases of VO<sub>2</sub>. In doing so we complement previous work on the rutile and M<sub>1</sub> phases by a more detailed analysis of their electronic properties, and we present new results for the M<sub>2</sub> phase [22].

The purpose of this work is twofold. First, by investigating a large class of related

compounds within the same theoretical approach, we are able to develop a more comprehensive understanding of the relevant mechanisms. Second, our density functional calculations benefit from the fact that they do not depend on adjustable parameters. Hence, despite possible limitations arising from the local density approximation, they establish a reference, which can be directly compared to experimental data. Finally, our results can be used as the starting point for more elaborate treatments, as e.g. the LDA+DMFT approach, which only recently has proven very successful in modelling the symmetry conserving metal-insulator transition of  $V_2O_3$  [25, 26].

The paper is organized as follows: In Sec. 2, an overview of previous results for  $VO_2$  is presented. In Sec. 3, the crystal structures of the different phases are described. Sec. 4 summarizes the gross features of our calculational method. In Secs. 5, 6, and 7 we discuss the results obtained for the rutile,  $M_1$ , and  $M_2$  phases, respectively. Finally, a summary is given in Sec. 8.

## 2 Summary of previous results for $VO_2$

### 2.1 Experimental results

The important role of the lattice degrees of freedom for the stabilization of the different phases of  $VO_2$  has been deduced from several experiments, which revealed striking differences between the metallic and the insulating state. Together with the symmetry change at the metal-insulator transition these findings were taken as evidence for strong electron-phonon coupling and a lattice softening at the transition [27]. Of course, this became most obvious from the fact that crystals could even break at the transition [28, 2]. Furthermore, X-ray measurements revealed large thermal displacements in the rutile phase of both stoichiometric and Cr-doped  $VO_2$ , which exceed the values measured in the respective low-temperature phases as well as in the neighbouring rutile compounds  $TiO_2$  and  $CrO_2$  considerably [20, 27]. Rao *et al.* observed a large anisotropy of the thermal expansion in the rutile phase ( $\alpha_{\parallel} \approx 5 - 6 \times \alpha_{\perp}$ ) [29, 30], which causes a strong temperature dependence of the electric field gradient at the vanadium site [31]. In addition, an anisotropic change of the lattice constants at the phase transition was reported [32, 30]: While the rutile  $c$  axis increases by  $\approx 1\%$  the  $a$  axis decreases by  $\approx 0.6\%$ . At the same time, the volume changes discontinuously by  $-0.044\%$  and the thermal expansion coefficient drops by a factor of three [33, 30]. Ultrasonic microscopy revealed a strong elastic anisotropy in the metallic phase, which disappears almost completely in the insulating state [34]. X-ray diffuse scattering measurements performed just above the metal-insulator transition by Terauchi and Cohen [35] indicated a lattice instability at the tetragonal R-point with a wave vector parallel to  $\Gamma$ -R and a polarization vector parallel to the  $c$  axis. This result confirmed the symmetry analysis by Brews, who showed the rutile-to-monoclinic transition to be compatible with a phonon instability at the R-point [36]. Indeed, using a shell model to calculate the phonon dispersion of several rutile-type compounds, Gervais and Kress found a phonon softening at the tetragonal R-point for  $VO_2$  [37]. Furthermore, the analysis of the eigenvectors of the R-point soft mode resulted in a displacement pattern of the metal atoms equivalent to that of the monoclinic phase [37]. Finally, an oxygen

isotope effect was observed for the transition temperature [38].

The electronic structure of metallic VO<sub>2</sub> has been probed by optical and photoemission experiments. According to optical measurements by Verleur *et al.* the lowest unfilled V 3*d* levels lie about 2.5 eV above the top of the O 2*p* bands [39]. This result was supported by photoemission measurements by Powell *et al.* [40]. UPS and XPS experiments revealed an  $\approx 8.5$  eV wide occupied band falling into the low binding, approximately 1.5 eV wide V 3*d* band and an  $\approx 6$  eV wide group of O 2*p* bands at higher binding energies [41, 42, 43, 44, 45]. According to O K-edge XAS experiments, the unoccupied V 3*d* bands extend from  $E_F$  to 1.7 eV and from 2.2 to 5.2 eV [46, 41, 47, 42, 45, 48]. The nearly isotropic electrical conductivity, which is only twice as large parallel to the rutile *c* axis as compared to its in-plane value [49, 50], has been attributed to the existence of at least two different bands near the Fermi energy and a rather complex Fermi surface [51]. The same conclusion was drawn from optical, Seebeck coefficient and magnetization measurements [39, 51, 52]. For the insulating phase, photoemission studies revealed a sharpening and downshift of the occupied V 3*d* bands [46, 41, 42, 44, 45] relative to the metallic phase. XAS measurements showed a splitting of the lowest unoccupied 3*d* state [47, 48]. Finally, the vanadium atom pairing is reflected by the magnetic susceptibility, which shows Curie-Weiss behaviour above  $T_c$  and a nearly constant van Vleck-like contribution below  $T_c$  [50, 51].

## 2.2 Theoretical work

Theoretical approaches to the insulating ground state of VO<sub>2</sub> as well as to the metal-insulator transition range from phenomenological models to first principles studies. In a survey over oxides with octahedrally coordinated transition metals, Goodenough pointed out the important role of direct cation-cation interactions, which add to and often supersede the cation-anion-cation interactions [3]. If strong enough, the cation-cation interactions may give rise to a covalent-type bonding at low temperatures. This bonding would go along with a displacement of the metal atom away from the center of symmetry of the anion interstice as well as with a spin pairing of the bonding electrons. In the case of VO<sub>2</sub>, the latter would explain the observed Curie-Weiss behaviour above  $T_c$  and the small temperature-independent van Vleck susceptibility below  $T_c$  [50]. Since those *d* electrons, which are responsible for the metal-metal bonding, do not contribute to metallic conductivity, the phase transition may be from the metallic to the semiconducting state [3]. Subsequently, Kawakubo proposed that the metal-insulator transition might be due to electronic excitations from the bonding to the antibonding state [53]. Giving arguments for a linear dependence of the energy gap on the number of excited carriers Adler and Brooks demonstrated that a system with a half-filled conduction band will lower its total energy and enter an insulating state by developing either antiferromagnetic order or a crystalline distortion [4, 5].

Lateron, Goodenough presented a schematic energy band diagram for both the metallic and the insulating phase [6, 7]. Using electrostatic considerations for the effective ionic charges he placed the oxygen 2*p* levels well below the vanadium 3*d* states. The latter are subject to octahedral crystal field splitting into lower *t*<sub>2*g*</sub> and higher *e*<sub>g</sub> levels. Furthermore, the *t*<sub>2*g*</sub> states, which are located near the Fermi energy, are split into a *d*<sub>||</sub> state, which is directed along the rutile *c* axis, and the remaining  $\pi^*$

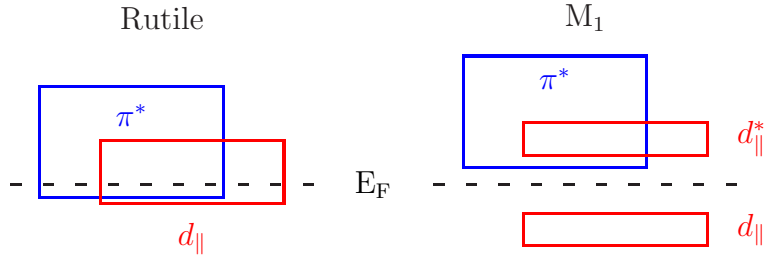


**Fig. 2** Schematic band diagrams for  $\text{VO}_2$ .

states, see Fig. 2. In the monoclinic phase, metal-metal pairing within the vanadium chains parallel to the rutile  $c$  axis causes splitting of the  $d_{\parallel}$  band into filled bonding and empty antibonding states. In contrast, the  $\pi^*$  bands move to higher energies due to the antiferroelectric zigzag-type displacement of the vanadium atoms. As a result, a band gap opens between the bonding  $d_{\parallel}$  band and the other  $t_{2g}$  bands. According to Shin *et al.* the  $d_{\parallel}$  band splitting amounts to  $\approx 2.5\text{eV}$ , while the  $\pi^*$  bands raise by  $\approx 0.5\text{eV}$  [41]. Nevertheless, in proposing this scheme Goodenough questioned the covalent-type bonding arising from metal-metal pairing as the major source of the phase transition. Instead, he suggested that the metal-insulator transition results predominantly from the increased  $p$ - $d$  overlap coming with the antiferroelectric distortion of the  $\text{VO}_6$  octahedra [6, 7]. It would lower and raise the bonding and antibonding  $\pi$  and  $\pi^*$  levels. The  $d_{\parallel}$  states would be split as a consequence of the symmetry change. Eventually this would open the optical band gap. Using the general band scheme sketched in Fig. 2, Hearn performed numerical calculations for one-dimensional vanadium chains and demonstrated the validity of the scenario outlined by Goodenough [54].

A mechanism differing from the molecular orbital picture of Goodenough was proposed by Zylbersztein and Mott. These authors attributed the coupled metal-insulator and structural transition to the presence of strong electron-electron correlations especially in the  $d_{\parallel}$  band rather than to electron-lattice interaction [11]. However, as Zylbersztein and Mott argue, these correlations are efficiently screened by the  $\pi^*$  bands in the metallic phase. In the insulating phase, the screening of the  $d_{\parallel}$  electrons is diminished since the  $\pi^*$  bands experience energetical upshift due to the antiferroelectric displacement of the V atoms. As a consequence, the narrow  $d_{\parallel}$  bands at the Fermi energy are susceptible to strong Coulomb correlations and undergo a Mott transition. This opens the optical band gap.

Lateron, Paquet and Leroux-Hugon presented a band model for  $\text{VO}_2$ , which aimed at incorporating both the electron-electron interactions and the electron-lattice coupling on an equal footing [12]. To do so, the authors started from a tight-binding representation for the  $d_{\parallel}$  and  $\pi^*$  bands. In addition, they included Hubbard-type interactions for both bands as well as a contribution due to the phonons. Using ex-

perimentally derived parameters Paquet and Leroux-Hugon concluded that the metal-insulator transition is primarily driven by electron-electron correlations. However, these correlations would be strongly renormalized by the lattice distortion and the electrostatic interaction between the  $d_{||}$  and the  $\pi^*$  electrons.

First principles studies for rutile VO<sub>2</sub> range from calculations using semiempirical or overlapping free atom potentials [55, 56] to self-consistent state-of-the-art investigations [57, 58, 8, 9, 22, 59]. Work on the insulating and monoclinic ( $M_1$ ) phase includes a semiempirical calculation [60], the molecular dynamics study by Wentzcovitch *et al.* [8, 9], state-of-the-art investigations using the LDA and LDA+U [22, 61], and a recent model GW calculation [62]. Most of these calculations confirmed the general molecular-orbital scheme sketched by Goodenough. They found the same order of bands for the metallic phase and related the change in electronic structure occurring at the phase transition to the simultaneous symmetry-lowering distortions of the crystal structure. From a maximum in the generalized susceptibility occurring at the tetragonal R-point, which could be traced back exclusively to the  $d_{||}$  bands, Gupta *et al.* concluded that the phase transition could be due to formation of a charge-density wave accompanied by a periodic lattice distortion leading to the monoclinic  $M_1$  structure [56]. Support for the predominant influence of the lattice degrees of freedom on the transition came from first principles molecular dynamics calculations by Wentzcovitch *et al.* [8]. Their variable cell shape approach allowed for simultaneously relaxing the atomic positions and the primitive translations. As a result, starting from different intermediate structures these authors obtained the monoclinic  $M_1$  structure as the most stable one. In addition, a slightly metastable rutile structure was found, which was about 54 meV per f.u. higher in energy as compared to the  $M_1$  structure. Calculated crystal structure parameters for both cells were in good agreement with the experimental data (see Sec. 3). However, the band structure obtained for monoclinic VO<sub>2</sub> contrasted the experimental finding of an 0.6 eV wide insulating gap [39, 63, 46, 41]. Instead, semimetallic behaviour with a band overlap of 0.04 eV was found [8]. This result was attributed to the typical failure of the local density approximation to correctly reproduce measured optical band gaps. The situation is thus not unlike that in small band gap semiconductors as Ge, where use of the local density approximation likewise leads to a metallic ground state. Wentzcovitch *et al.* suspected that, by further strengthening the V-V bonds, the gap should eventually open and, hence, VO<sub>2</sub> could be regarded as a band insulator. This was interpreted as assertion of the energy band scheme by Goodenough [6, 7]. More recent studies using the local density approximation confirmed the results presented by Wentzcovitch *et al.* in that they also found semimetallic rather than semiconducting behaviour [22, 59]. Nevertheless, a recent LDA+U approach and a quasiparticle band structure calculation as based on a model GW scheme produced the correct optical band gap [61, 62].

Despite the huge amount of theoretical investigations there still remain fundamental questions. First of all, none of the previous studies has presented a detailed analysis of the band structure or the density of states in terms of the orbitals discussed by Goodenough. For this reason, the molecular orbital considerations as well as the more recent model approaches lack a profound justification. In addition, most of the previous studies, including those of Goodenough as well as Zylbersztejn and Mott, emphasize the role of the  $\pi^*$  bands for the transition. Yet, as will be discussed in

more detail in Sec. 3, the role of the zigzag-like displacement of the metal atoms for the metal-insulator transition is still unclear. This is related to the different response of the surrounding oxygen atoms. In  $\text{VO}_2$ , the oxygen atoms stay essentially at their original positions and the vanadium atom shifts lead to an increased metal-oxygen bonding. This causes an energetical upshift of the  $\pi^*$  bands. In contrast, in  $\text{MoO}_2$  the metal atom displacements are to a large part compensated by the accompanying shift of the oxygen octahedron. As a consequence, the zigzag-like displacement of the metal atoms does not lead to an increased metal-oxygen bonding. As a consequence, it does not generally act as an antiferroelectric mode. Hence, the zigzag-like displacement cannot be regarded as a common origin for the destabilization of the rutile structure.

### 2.3 The $M_2$ phase

The understanding of  $\text{VO}_2$  and the metal-insulator transition is even more complicated due to the presence of two additional phases of this material. They appear on application of uniaxial stress or on doping of  $\text{VO}_2$  with small amounts of Cr, Fe, Al, or Ga of the order of few percent [20, 31, 2]. The phase diagram of Cr doped  $\text{VO}_2$  as given by Pouget and Launois [31] is shown in Fig. 3. This phase diagram differs slightly from

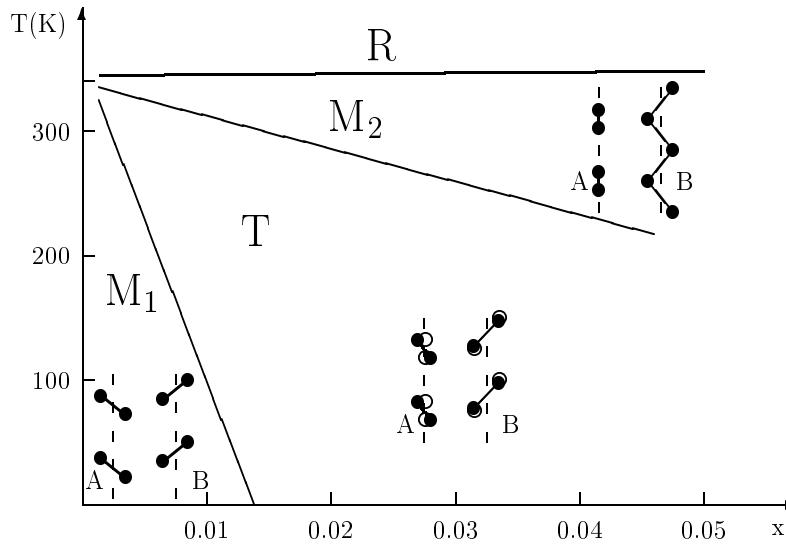


**Fig. 3** Phase diagram of  $\text{V}_{1-x}\text{Cr}_x\text{O}_2$  according to Pouget and Launois [31]. The distortion patterns of the metallic chains are given in the insets (open circles in the T phase refer to the positions of the  $M_2$  phase).

that given by other authors, which fact has been attributed to differences in sample preparation and stoichiometry [20, 64]. Lateron, a similar phase diagram was reported for  $\text{V}_{1-x}\text{Al}_x\text{O}_2$  by Ghedira *et al.* [65, 66]. According to Fig. 3, Cr-doped  $\text{VO}_2$  enters, on cooling, the monoclinic  $M_2$  phase in a first order metal-insulator transition [64]. On further lowering of the temperature, transition to the triclinic T phase occurs, which, for chromium concentrations smaller than 0.015, is followed by a first order transition

to the monoclinic M<sub>1</sub> phase [20]. According to X-ray measurements by Marezio *et al.*, each of the three low-temperature phases shows a particular distortion pattern of the atomic arrangement especially of the characteristic vanadium chains [20]. Whereas in the M<sub>1</sub> phase both the metal-metal pairing and the zigzag-type lateral displacement are observed on each chain, in the M<sub>2</sub> phase only half of the chains dimerize and the zigzag-type deviations are reserved to the other half of the chains. Finally, the T phase is intermediate, as those chains, which in the M<sub>2</sub> phase dimerize, gradually start to tilt, whereas the zigzag chains start to dimerize until distortions in both chains are identical and eventually the M<sub>1</sub> phase is reached. Hence, the T and M<sub>1</sub> phases can be regarded as superpositions of two M<sub>2</sub>-type displacements with unequal and equal weights, respectively. The role of the latter displacement pattern as the “fundamental” one may be understood from the symmetry considerations presented by Pouget *et al.* as well as by Paquet and Leroux-Hugon [64, 12, 13]. According to these ideas the pairing on one chain is intimately connected with the zigzag-type displacement on the neighbouring chains: If the vanadium atoms pair on one chain, the atoms on the neighbouring chains, which from the outset are vertically displaced by half the rutile *c* axis, move off the chain axis towards the apical oxygen atom whose V neighbours of the first sublattice have pulled apart. For this reason, the zigzag-like displacement may be viewed as being coupled to the metal-metal pairing along the rutile *c* axis.

V<sup>51</sup>-NMR measurements by Pouget *et al.* confirmed the X-ray experiments performed by Marezio *et al.*. They revealed a positive Knight shift for the M<sub>1</sub> phase of V<sub>1-x</sub>Cr<sub>x</sub>O<sub>2</sub>, which is similar to that of pure VO<sub>2</sub>. In contrast, both a positive and a negative Knight shift were observed in the M<sub>2</sub> phase indicating two different types of vanadium atoms [64]. Whereas the positive Knight shift again points to paired V sites the negative Knight shift gives evidence for V<sup>4+</sup> atoms with localized 3*d* electrons. Finally, as D’Haenens *et al.* found from ESR data, the chromium atoms enter as substitutional Cr<sup>3+</sup> ions on the zigzag-type chains [67, 68].

Magnetic susceptibility curves taken by Pouget *et al.* for V<sub>1-x</sub>Cr<sub>x</sub>O<sub>2</sub> showed a striking similarity to corresponding data for Fe-doped VO<sub>2</sub> as measured by Kosuge [50]. They could be decomposed into a van Vleck contribution for the paired vanadium chains, a Curie-Weiss term representing the Cr<sup>3+</sup> spins and an almost constant residual term. Using a model by Bonner and Fisher [69], Pouget *et al.* were able to attribute the latter contribution to noninteracting spin- $\frac{1}{2}$  linear Heisenberg chains, formed by the equispaced vanadium atoms, with an exchange constant of the order of room temperature [64]. The M<sub>2</sub> to T transition was thus viewed as a bonding or dimerization transition of a linear Heisenberg chain. This interpretation was confirmed by the observed decrease of the magnetic susceptibility at the transition, which is accompanied by an increase of the electrical conductivity by a factor of two [66]. From the existence of well localized 3*d* electrons at the V<sup>4+</sup> sites, Pouget *et al.* concluded that the results should be interpreted in terms of a Mott-Hubbard-type picture. In doing so, they attributed the insulating gap to electronic correlations [64].

Later on, Pouget *et al.* demonstrated that both the M<sub>2</sub> and T phase could be likewise stabilized by applying uniaxial stress along either the [110] or the [1 $\bar{1}$ 0] direction in stoichiometric VO<sub>2</sub> samples [70]. Such uniaxial stress can be viewed as suppressing the zigzag-type displacements on those chains, which have their tilting along the direction of the applied stress, while the respective other chains are not affected. How-

ever, from the above symmetry considerations it follows that, as a consequence of the reduced tilt on one half of the chains, the pairing on the other chains will be also reduced. Additional NMR and EPR data revealed that the local symmetries as well as the magnetic properties of the two vanadium sites are identical in pure  $\text{VO}_2$  under uniaxial stress and in  $\text{V}_{1-x}\text{Cr}_x\text{O}_2$  [70].

As Pouget *et al.* pointed out, the critical uniaxial stress for appearance of the  $\text{M}_2$  phase is so small that the free energies of the  $\text{M}_1$  and  $\text{M}_2$  phases in pure  $\text{VO}_2$  must be extremely close at temperatures just below the metal-insulator transition [70]. The same conclusion was drawn by Pouget *et al.* for doped  $\text{VO}_2$ . These authors pointed to the fact that, although the  $\text{M}_2$  and T phases involve substantial changes in the vanadium atom positions, they could be stabilized by impurity concentrations as low as 0.2% [64]. According to Pouget *et al.* the  $\text{M}_2$  and the T phase thus must be interpreted as alternative phases of pure  $\text{VO}_2$  whose free energies are only slightly higher than that of the  $\text{M}_1$  phase of the pure material [64]. As a consequence, the  $\text{M}_2$  phase was regarded as a metastable modification of the  $\text{M}_1$  phase. In contrast, the T phase appears as a transitional state, which displays characteristics of both monoclinic phases.

The discovery of the  $\text{M}_2$  phase with its two different types of vanadium chains was difficult to reconcile with all those theoretical approaches, which had explained the insulating ground state as originating from crystal structure distortions with a predominant influence of either the pairing or the zigzag-type displacement. Furthermore, from the presence of localized  $3d$  electrons on the zigzag chains and the antiferromagnetic ordering of the local moments within non-interacting linear Heisenberg chains many authors concluded that band theory were unable to correctly describe the physics of the  $\text{M}_2$  and, hence, also of the  $\text{M}_1$  phase. Instead, electronic correlations were regarded as essential and localized models called for [64, 11, 13]. Yet, an explanation of the physics of  $\text{VO}_2$  purely in terms of a Mott-Hubbard-type picture might be difficult in view of the complex structural changes at the metal-insulator transitions, which lead to the same crystal structures as those of the neighbouring metallic transition-metal dioxides.

Although, as Rice *et al.* have pointed out again only recently [13], discussion of the monoclinic  $\text{M}_2$  phase of  $\text{VO}_2$  is essential for a comprehensive understanding of the physics underlying the metal-insulator transition, state-of-the-art first principles calculations for this phase did not seem to exist. In order to close this gap we included an investigation of the monoclinic  $\text{M}_2$  phase in the present study [22]. Again, our aim is to provide an as broad as possible picture of the physics of the rutile-type transition metal oxides using a well defined first principles approach.

To be specific, since the low-temperature  $\text{M}_1$  and  $\text{M}_2$  phases involve characteristic but still relative small deviations from the rutile phase we follow the lines of our work on  $\text{MoO}_2$  and  $\text{NbO}_2$  and start out investigating the rutile structure [23, 24]. The results will then serve as a reference for the subsequent investigation of the low-temperature phases.

### 3 Crystal structures and local coordinate systems

#### 3.1 Rutile structure

The rutile structure of metallic VO<sub>2</sub> is based on a simple tetragonal lattice with space group  $P4_2/mnm$  ( $D_{4h}^{14}$ , No. 136) [71, 27]. The metal atoms are located at the Wyckoff positions (2a):  $(0, 0, 0)$ ,  $(\frac{1}{2}, \frac{1}{2}, \frac{1}{2})$  and the oxygen atoms occupy the positions (4f):  $\pm(u, u, 0)$ ,  $\pm(\frac{1}{2} + u, \frac{1}{2} - u, \frac{1}{2})$ . The rutile structure is displayed in Fig. 4. According

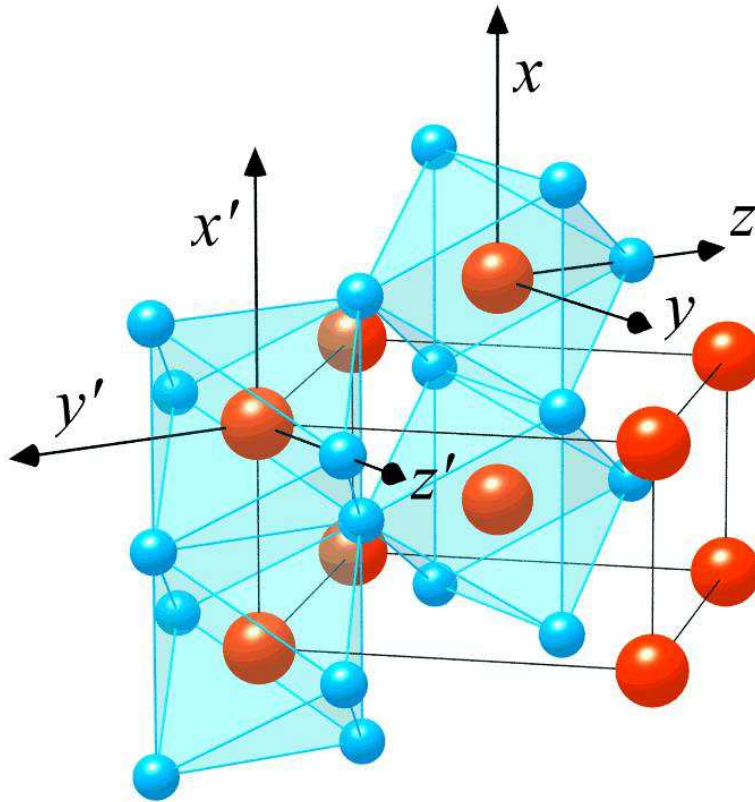


**Fig. 4** The rutile structure. Large and small spheres denote metal and ligand atoms, respectively.

to McWhan *et al.* the lattice constants and the internal oxygen parameter are  $a_R = 4.5546 \text{ \AA}$ ,  $c_R = 2.8514 \text{ \AA}$  and  $u = 0.3001$  [27]. These numbers will be used in the calculations. While Westman reported slightly different lattice parameters for metallic VO<sub>2</sub> [71], the numbers by McWhan *et al.* are in very close agreement with the values given by Marezio *et al.* for V<sub>0.976</sub>Cr<sub>0.024</sub>O<sub>2</sub> ( $u = 0.3004$ ) as well as with those by Ghedira *et al.* for VO<sub>2</sub> doped with 1.5% of Al ( $a_R = 4.5546 \text{ \AA}$ ,  $c_R = 2.8528 \text{ \AA}$  and  $u = 0.3001$ ) [20, 66]. Finally, we mention the parameters resulting from the first principles molecular dynamics calculations by Wentzcovitch *et al.*,  $a_R = 4.58 \text{ \AA}$ ,  $c_R = 2.794 \text{ \AA}$

and  $u = 0.3000$ , which differ only slightly from the experimental values [8].

As has been already outlined in our previous work on  $\text{MoO}_2$  [23], the rutile structure can be alternatively visualized in terms of a body-centered tetragonal lattice formed by the metal atoms, where each metal atom is surrounded by an oxygen octahedron. Octahedra centered at the corners and the center of the cell are rotated by  $90^\circ$  about the tetragonal  $c$  axis relative to each other. As a consequence, the lattice translational symmetry reduces to simple tetragonal. Thus, the unit cell contains two formula units. Octahedra neighbouring along the rutile  $c$  axis, share edges whereas the resulting octahedral chains are interlinked via corners. Each octahedron has orthorhombic symmetry. Yet, the deviations from tetragonal and even cubic geometry are rather small for most compounds and still allow for a discussion in terms of the latter. There exist two different metal-oxygen distances. The apical distance is between metal and oxygen atoms having the same  $z$  value. The equatorial distance is between the metal atom and the four neighbouring ligand atoms with  $z = z_{\text{metal}} \pm 1/2$  [15, 16, 72].

As we will realize in the following sections it is useful to discuss the electronic structure of rutile-type compounds in terms of local coordinate systems centered at each metal site. These coordinate systems have been already indicated in Fig. 4. Note that due to the different orientation of octahedra centered at the corner and in the center of the rutile cell, the local  $z$  axes point alternately along the  $[110]$  and  $[\bar{1}\bar{1}0]$  direction. In contrast to the usual adjustment of the  $x$  and  $y$  axes parallel to the metal-ligand bonds we have rotated these axes by  $45^\circ$  about the local  $z$  axes such that they are parallel and perpendicular, respectively, to the rutile  $c$  axis.

In Fig. 5, we show the angular parts of the metal  $d$  orbitals relative to the local reference frame of the central metal atom. With the previous choice of local coordinate systems the  $e_g$  states resulting from the cubic part of the crystal field splitting of the metal  $d$  orbitals comprise the  $d_{3z^2-r^2}$  and  $d_{xy}$  orbitals. In contrast, the  $t_{2g}$  states are built from the  $d_{x^2-y^2}$ ,  $d_{xz}$ , and  $d_{yz}$  orbitals. While the  $d_{x^2-y^2}$  orbitals point along the rutile  $c$  and the local  $y$  axes, i.e. towards the edges of the basal plane of the octahedron, the  $d_{xz}$  and  $d_{yz}$  orbitals are directed towards the faces. In particular, the  $d_{yz}$  states point along the  $\langle 100 \rangle$  directions. As a consequence, the  $d_{x^2-y^2}$  and  $d_{xz}$  orbitals mediate  $\sigma$ - and  $\pi$ -type overlap, respectively, between metal sites within the vertical chains formed by the octahedra. In contrast, the  $d_{yz}$  orbitals have an albeit smaller  $\sigma$ -type overlap with their counterparts at metal sites translated by the vectors  $\langle 1, 0, 0 \rangle$ . This is due to the above  $45^\circ$  rotation of the local coordinate system. This additional rotation interchanges the  $d_{x^2-y^2}$  and  $d_{xy}$  orbitals and adjusts the  $d_{yz}$  orbitals parallel to the axes of the rutile basal plane. The overlap of both the  $d_{x^2-y^2}$  and  $d_{yz}$  orbitals with orbitals of the same kind at neighbouring atoms thus connects atoms, which are separated by lattice vectors of the simple tetragonal lattice. In contrast, coupling between metal atoms, which are located at the corner and in the center of the cell, is mediated by the  $d_{xz}$  orbitals. These orbitals point to the voids between the metal atoms of the neighbouring octahedral chains where they overlap with the  $d_{x^2-y^2}$  orbitals of these chains.

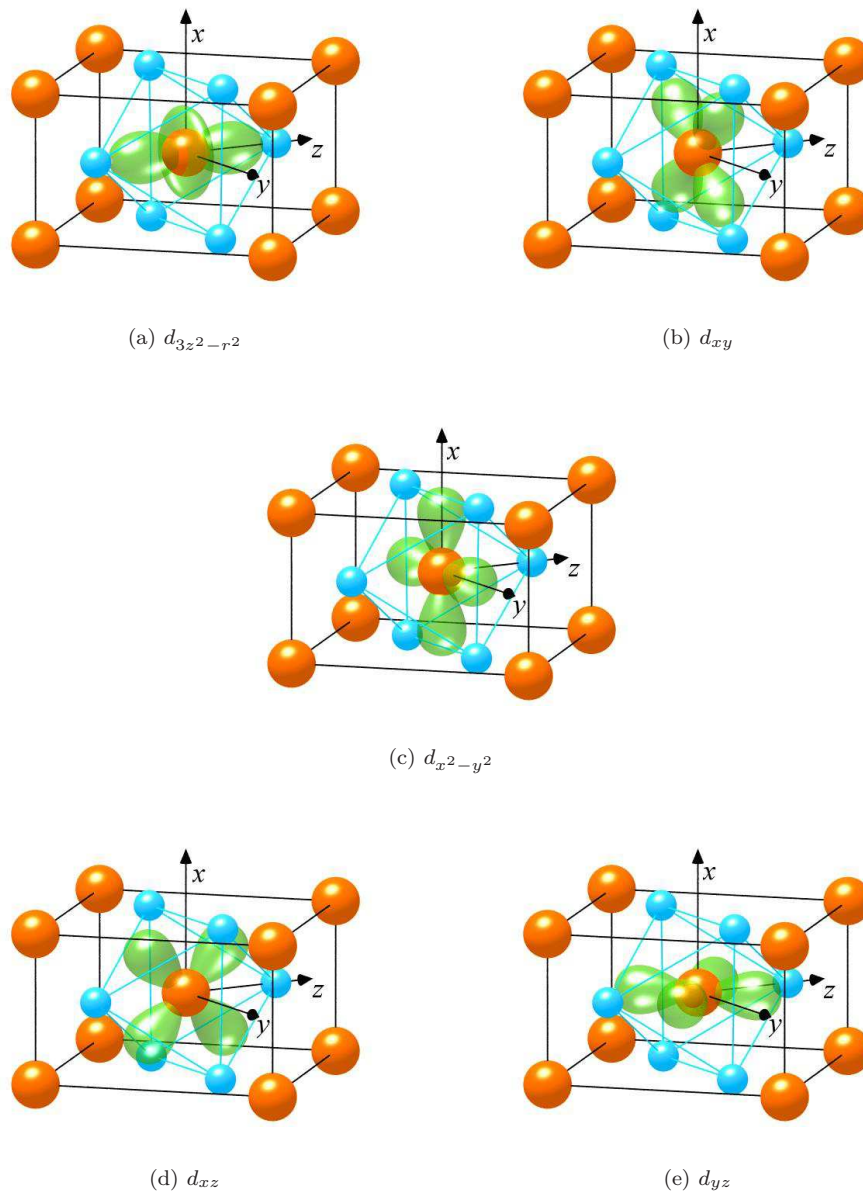


**Fig. 5** Angular parts of the  $d$  orbitals.

### 3.2 The $M_1$ structure

The monoclinic  $M_1$  structure of stoichiometric  $\text{VO}_2$  is characterized by a simple monoclinic lattice with space group  $P2_1/c$  ( $C_{2h}^5$ , No. 14) [18, 19]. According to Andersson the lattice constants and the monoclinic angle are  $a_{M_1} = 5.743 \text{ \AA}$ ,  $b_{M_1} = 4.517 \text{ \AA}$ ,  $c_{M_1} = 5.375 \text{ \AA}$ , and  $\beta_{M_1} = 122.61^\circ$ , respectively [18]. Lateron, Longo and Kierkegaard reported values  $a_{M_1} = 5.7517 \text{ \AA}$ ,  $b_{M_1} = 4.5378 \text{ \AA}$ ,  $c_{M_1} = 5.3825 \text{ \AA}$ , and  $\beta_{M_1} = 122.646^\circ$ , respectively [19], which will be used in the subsequent calculations. The crystal structure is displayed in Fig. 6. The unit cell comprises four formula units. The metal

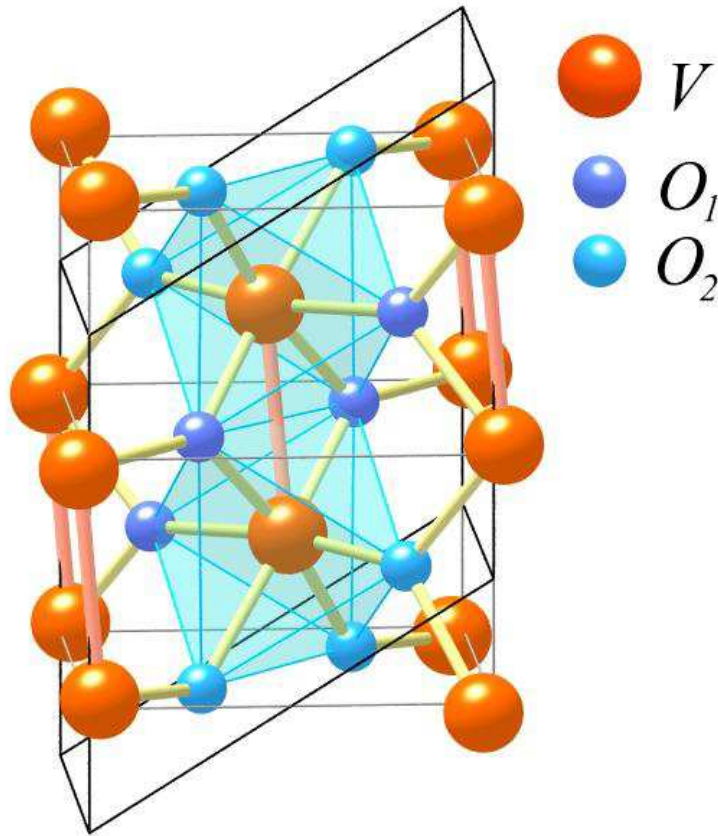


**Fig. 6** Monoclinic  $M_1$  structure of  $\text{VO}_2$ .

atoms as well as the two different types of oxygen atoms occupy the general Wyckoff position (4e):  $\pm(x, y, z)$ ,  $\pm(x, \frac{1}{2} - y, \frac{1}{2} + z)$ . The latter are referred to the standard choice

$$\mathbf{a}_{M_1,1} = \begin{pmatrix} 0 \\ 0 \\ -a_{M_1} \end{pmatrix}, \quad \mathbf{a}_{M_1,2} = \begin{pmatrix} -b_{M_1} \\ 0 \\ 0 \end{pmatrix}, \quad \mathbf{a}_{M_1,3} = \begin{pmatrix} 0 \\ c_{M_1} \sin \beta_{M_1} \\ -c_{M_1} \cos \beta_{M_1} \end{pmatrix} \quad (1)$$

for the primitive translations. The atomic positions given by Andersson as well as by Longo and Kierkegaard are listed in Tables 2 and 3. Note that all positions have been

**Table 2** Crystal structure parameters of M<sub>1</sub>-VO<sub>2</sub> as given by Andersson (from Ref. [18]).

Atom	Wyckoff positions	parameters		
		$x$	$y$	$z$
V	(4e)	0.242	0.975	0.025
O <sub>1</sub>	(4e)	0.10	0.21	0.20
O <sub>2</sub>	(4e)	0.39	0.69	0.29

**Table 3** Crystal structure parameters of M<sub>1</sub>-VO<sub>2</sub> as given by Longo and Kierkegaard (from Ref. [19]).

Atom	Wyckoff positions	parameters		
		$x$	$y$	$z$
V	(4e)	0.23947	0.97894	0.02646
O <sub>1</sub>	(4e)	0.10616	0.21185	0.20859
O <sub>2</sub>	(4e)	0.40051	0.70258	0.29884

shifted by half of the rutile  $c$  axis, i.e. quarter of the monoclinic  $a$  axis as compared to the high-temperature data.

Again we complement the measured crystal structure parameters by those resulting from the variable cell shape molecular dynamics calculations by Wentzcovitch *et al.* [8, 9]. These authors reported lattice constants  $a_{M_1} = 5.629 \text{ \AA}$ ,  $b_{M_1} = 4.657 \text{ \AA}$ ,  $c_{M_1} = 5.375 \text{ \AA}$ , and a monoclinic angle  $\beta_{M_1} = 122.56^\circ$ , respectively [8]. The calculated atomic parameters are listed in Table 4. As for the rutile structure the agreement

**Table 4** Crystal structure parameters of M<sub>1</sub>-VO<sub>2</sub> as given by Wentzcovitch *et al.* (from Ref. [8]).

Atom	Wyckoff positions	parameters		
		$x$	$y$	$z$
V	(4e)	0.233	0.976	0.021
O <sub>1</sub>	(4e)	0.118	0.212	0.228
O <sub>2</sub>	(4e)	0.399	0.685	0.293

with the measured values is very good. With only few small exceptions all calculated numbers are within the range spanned by the two sets of experimental data, which by themselves show some variation.

The close relationship of the monoclinic  $M_1$  structure to the high-temperature rutile structure becomes visible from a comparison of Fig. 6 to Fig. 4. Furthermore, comparing the lattice parameters of the rutile and  $M_1$  structures we realize that the primitive translations of the latter can be approximately written as

$$\mathbf{a}_{M_1,1} \approx \begin{pmatrix} 0 \\ 0 \\ -2c_R \end{pmatrix}, \quad \mathbf{a}_{M_1,2} \approx \begin{pmatrix} -a_R \\ 0 \\ 0 \end{pmatrix}, \quad \mathbf{a}_{M_1,3} \approx \begin{pmatrix} 0 \\ a_R \\ c_R \end{pmatrix}. \quad (2)$$

This representation emphasizes the prescription of the monoclinic cell in terms of a rutile cell doubled along the rutile  $c$  axis.

Nevertheless, as for  $\text{MoO}_2$  and  $\text{NbO}_2$  there exist three distinct differences between both structures: i) In Fig. 6 we observe the characteristic metal-metal pairing along the rutile  $c$  axis. It gives rise to two different metal-metal distances of 2.619 and 3.164 Å, which contrast the average value of 2.851 Å assumed in the rutile structure. ii) We witness the zigzag-like in-plane displacements of the vanadium atoms parallel to the local  $z$  axis, hence, parallel to the diagonal of the rutile basal plane. These shifts likewise alternate along both the tetragonal  $a$  and  $c$  axis. As a consequence of the zigzag-like distortion two different apical vanadium oxygen bond lengths of 1.77 and 2.01 Å arise. In contrast, the metal atom pairing leads to two short and two long equatorial V–O bond lengths of 1.86, 1.89, 2.03, and 2.06 Å. iii) There is a lattice strain which causes deviations of the ratios

$$\frac{c_{M_1} \sin \beta_{M_1}}{b_{M_1}} = 0.9988, \quad \frac{-2c_{M_1} \cos \beta_{M_1}}{a_{M_1}} = 1.0096$$

from unity.

Despite the many similarities of the monoclinic structures of  $\text{MoO}_2$  and  $\text{VO}_2$  a more detailed analysis of the crystal structure data reveals striking differences between both compounds. They regard the zigzag-like in-plane displacements of the metal atoms and the distortions of the surrounding oxygen octahedra: i) In  $\text{MoO}_2$  the in-plane shift makes an angle of  $18^\circ$  with the local  $z$  axis. In contrast, the vanadium atoms, in addition to dimerizing along the rutile  $c$  axis, experience in-plane shifts, which are parallel to the local  $z$  axis, hence, parallel to the  $\langle 110 \rangle$  direction. ii) Even more striking is the different response of the oxygen sublattice to the displacements of the metal atoms. In  $\text{VO}_2$  the oxygen atoms do not follow the metal atom shifts and stay almost at their original positions. In contrast, the oxygen atoms in  $\text{MoO}_2$ , while hardly moving parallel to the rutile  $c$  axis, follow the lateral displacements of the molybdenum atoms to a large degree. Hence, in  $\text{VO}_2$  the lateral displacement of the vanadium atoms causes a shift *relative* to the rather fixed oxygen octahedra such that the  $p$ - $d$ -like metal-oxygen bonding is affected. This is different in  $\text{MoO}_2$ , where the molybdenum atom displacements are compensated to a large degree by the simultaneous shift of the surrounding oxygen atoms. In other words, the zigzag-type in-plane displacement of the metal atoms does not automatically lead to an (anti)ferroelectric distortion of the whole octahedron, but may still be compensated by a corresponding

displacement of the surrounding oxygen cage. Nevertheless, according to the symmetry considerations pointed out e.g. by Paquet and Leroux-Hugon, the zigzag-type shift is still coupled to the vertical metal-metal pairing. The previous observation and especially the different behaviour of the two dioxides has strong implications for our understanding of the whole class of materials. As has been discussed in Sec. 2, the lateral zigzag-like displacement of the metal atoms could lead to energetical upshift of the  $\pi^*$  bands. However, if compensated by accompanying oxygen displacements, this antiferroelectric mode is deactivated and the  $\pi^*$  bands stay at their original position. This has indeed been observed in our calculations for MoO<sub>2</sub> [23]. We are thus led to the conclusion that the antiferroelectric mode can not explain the tendency of the transition-metal dioxides to form distorted variants of the rutile structure. For the same reason, this mode must be excluded as the driving force for the metal-insulator transition, which is intimately connected to the destabilization of rutile. These observations are difficult to reconcile with the scenarios sketched by Goodenough as well as Zylbersztejn and Mott [6, 7, 11]

### 3.3 The $M_2$ structure

In the  $M_2$  phase, VO<sub>2</sub> crystallizes in a centered monoclinic lattice with space group  $C2/m$  ( $C_{2h}^3$ , No. 12) [20, 66]. In contrast to the monoclinic  $M_1$  structure, this time the monoclinic angle distorts the basal plane of the original rutile cell and, hence, the setup of the new primitive translations is different from that of the  $M_1$  phase. Usually, the crystal structure of the  $M_2$  phase is specified in terms of the underlying *simple* monoclinic lattice as defined by the primitive translations [20]

$$\mathbf{a}_{M_2,1} = \begin{pmatrix} a_{M_2} \\ 0 \\ 0 \end{pmatrix}, \quad \mathbf{a}_{M_2,2} = \begin{pmatrix} 0 \\ 0 \\ b_{M_2} \end{pmatrix}, \quad \mathbf{a}_{M_2,3} = \begin{pmatrix} c_{M_2} \cos \beta_{M_2} \\ -c_{M_2} \sin \beta_{M_2} \\ 0 \end{pmatrix}. \quad (3)$$

The lattice constants and monoclinic angle as resulting from the single crystal measurements on V<sub>0.976</sub>Cr<sub>0.024</sub>O<sub>2</sub> by Marezio *et al.* are  $a_{M_2} = 9.0664 \text{ \AA}$ ,  $b_{M_2} = 5.7970 \text{ \AA}$ ,  $c_{M_2} = 4.5255 \text{ \AA}$ , and  $\beta_{M_2} = 91.88^\circ$ , respectively [20]. There exist two different types of metal atoms and three types of oxygens, which occupy subsets of the general Wyckoff position (8j):  $\pm(x, y, z)$ ,  $\pm(x, -y, z)$ ,  $(\frac{1}{2}, \frac{1}{2}, 0) \pm(x, y, z)$ , and  $(\frac{1}{2}, \frac{1}{2}, 0) \pm(x, -y, z)$ . The parameters given by Marezio *et al.*, which will be used in the calculations below, are listed in Table 5. Ghedira *et al.*, who performed single crystal measurements on VO<sub>2</sub> doped with 1.5% of aluminum, also found a simple monoclinic lattice with lattice constants  $a_{M_2} = 9.060 \text{ \AA}$ ,  $b_{M_2} = 5.800 \text{ \AA}$ ,  $c_{M_2} = 4.5217 \text{ \AA}$ , monoclinic angle  $\beta_{M_2} = 91.85^\circ$ , and the atomic positions listed in Table 6 [65, 66]. The striking close agreement of both data sets supports the interpretation of the  $M_2$  phase as a metastable modification of the  $M_1$  phase, which hardly depends on the dopant and the amount of doping. As already mentioned, the  $M_2$  phase can be likewise stabilized by the application of uniaxial pressure along the [110] direction [70]. Unfortunately, no crystal structure data exist for this situation.

For the purpose of the present work we prefer using the related centered monoclinic lattice, which comprises four instead of eight formula units. An alternative

**Table 5** Crystal structure parameters of the  $M_2$  phase of  $V_{0.976}Cr_{0.024}O_2$  as given by Marezio *et al.* [20].

Atom	Wyckoff positions	parameters		
		$x$	$y$	$z$
$V_1$	(4g)	0.0	0.7189	0.0
$V_2$	(4i)	0.2314	0.0	0.5312
$O_1$	(8j)	0.1482	0.2475	0.2942
$O_2$	(4i)	0.3969	0.0	0.2089
$O_3$	(4i)	0.1000	0.0	0.7987

**Table 6** Crystal structure parameters of the  $M_2$  phase of  $V_{0.985}Al_{0.015}O_2$  as given by Ghedira *et al.* [66].

Atom	Wyckoff positions	parameters		
		$x$	$y$	$z$
$V_1$	(4g)	0.0	0.7189	0.0
$V_2$	(4i)	0.2312	0.0	0.5311
$O_1$	(8j)	0.1460	0.2474	0.2865
$O_2$	(4i)	0.3975	0.0	0.2284
$O_3$	(4i)	0.0980	0.0	0.7862

representation of this lattice originates from a redefinition of the first lattice vector as

$$\mathbf{a}_{M_2,1} = \frac{1}{2} \begin{pmatrix} a_{M_2} \\ 0 \\ b_{M_2} \end{pmatrix} \quad (4)$$

while  $\mathbf{a}_{M_2,2}$  and  $\mathbf{a}_{M_2,3}$  are the same as in Eq. (3). Using this definition and comparing the lattice constants of the rutile and the  $M_2$  phases we note the following approximate relation for the primitive translations [20]

$$\mathbf{a}_{M_2,1} \approx \begin{pmatrix} a_R \\ 0 \\ c_R \end{pmatrix}, \quad \mathbf{a}_{M_2,2} \approx \begin{pmatrix} 0 \\ 0 \\ 2c_R \end{pmatrix}, \quad \mathbf{a}_{M_2,3} \approx \begin{pmatrix} 0 \\ -a_R \\ 0 \end{pmatrix}. \quad (5)$$

They are equivalent to the vectors given in Eq. (2). Indeed, were it not for the lattice strain present in both low-temperature structures, which hinders writing the primitive translations as integer linear combinations of the rutile lattice vectors, the primitive translations of the  $M_1$  and  $M_2$  structure were identical (except for a rotation by  $90^\circ$  about the Cartesian  $z$  axis). This is a consequence of the fact that both monoclinic

phases result from the same R-point instability of the rutile phase. This has been pointed out by Brews [36] and by Blount (as mentioned by McWhan *et al.* [27]). As a consequence, we are able to use the same setup of Brillouin zones for both monoclinic lattices. This will facilitate our discussion of the band structures below. The close relationship between the two monoclinic phases becomes also obvious from Fig. 7, where we display the crystal structure of the M<sub>2</sub> phase using the unit cell spanned by

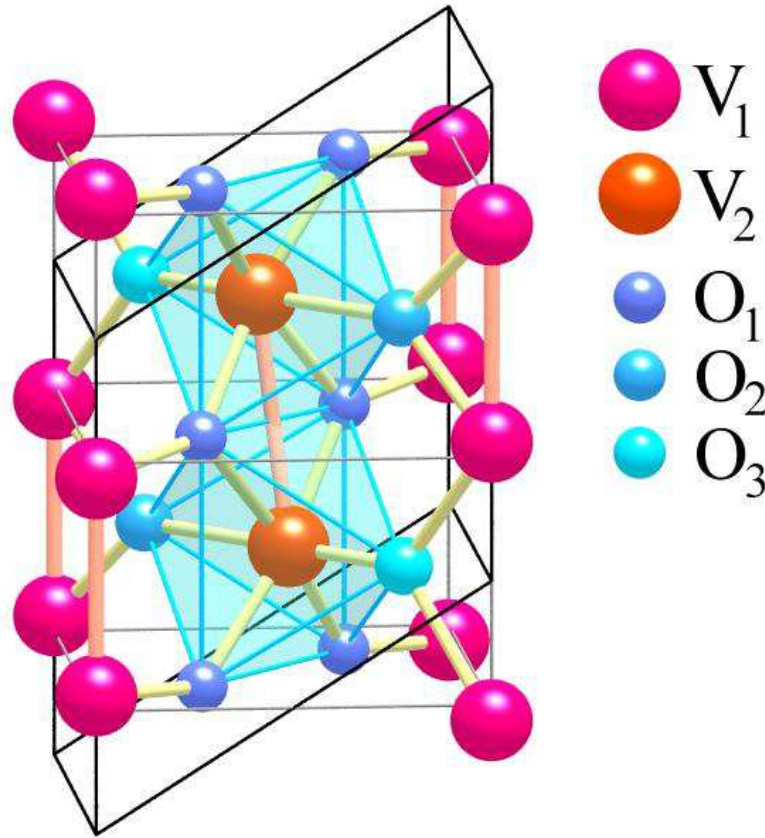


**Fig. 7** Monoclinic M<sub>2</sub> structure of VO<sub>2</sub>.

the lattice vectors (3) and (4). We identify the vanadium atoms V<sub>1</sub> and V<sub>2</sub> at the corners and centers, respectively, of the underlying stacked rutile cells. Oxygen atoms of type O<sub>1</sub> are located at the apices of the octahedra centered about vanadium atoms V<sub>1</sub>. They span the equatorial planes of the octahedra centered about vanadium atoms V<sub>2</sub>. In contrast, oxygen atoms of types O<sub>2</sub> and O<sub>3</sub> are equatorial atoms for V<sub>1</sub> and apical atoms relative to V<sub>2</sub>. Since the latter are shifted along the axis O<sub>2</sub>-V<sub>2</sub>-O<sub>3</sub> (see below) the identity of these two oxygen atoms is lost and two different apical V<sub>2</sub>-O bond lengths evolve.

As for the  $M_1$  structure, differences between the R and  $M_2$  phases arise from the distinct local deformations of the  $VO_6$  octahedra. Again, basic entities are i) the metal-metal pairing along the rutile  $c$  axis and ii) the zigzag-like in-plane displacements of the vanadium atoms parallel to the local  $z$  axis, hence, parallel to the diagonal of the rutile basal plane (see above). As in the  $M_1$  structure these shifts alternate along both the tetragonal  $a$  and  $c$  axis. Furthermore, the oxygen atoms hardly move such that the antiferroelectric mode causes a displacement of the vanadium atoms *relative* to the surrounding oxygen octahedron and is not suppressed as in  $MoO_2$ .

Yet, in contrast to the  $M_1$  phase, the above basic distortion patterns are not equally displayed by both chains. As already discussed in Sec. 2 and as is visible in Fig. 7, only half of the chains dimerize ( $V_1$  chains) while the other half ( $V_2$  chains) experiences the zigzag-like displacement without showing any pairing. As a consequence, two different  $V_1$ - $V_1$  bond lengths of 2.538 and 3.259 Å appear while there is only one  $V_2$ - $V_2$  bond length of 2.933 Å. Within the octahedra centered about  $V_1$  the two apical  $V_1$ - $O_1$  distances are 1.868 Å. Due to the vanadium-vanadium dimerization within these chains two short  $V_1$ - $O_2$  distances of 1.852 Å and two long  $V_1$ - $O_3$  distances of 2.089 Å arise. In contrast, in the octahedra centered about the tilted vanadium atoms the four equatorial  $V_2$ - $O_1$  bond lengths of 1.931 and 1.974 Å are very similar. At the same time, the distances between the central  $V_2$  atom and the apical  $O_2$  and  $O_3$  disproportionate and assume the values 2.127 and 1.726 Å.

Finally, we mention the lattice strain, which, in addition to the strains present in the  $M_1$  lattice, distorts the rutile basal plane. The resulting parallelogram would be likewise expected to result from uniaxial pressure along the [110] direction. It suppresses the zigzag-like displacement on those chains, which have their local  $z$  axes parallel to the shorter diagonal of the parallelogram. Since, according to the above symmetry arguments, the zigzag mode is connected to the dimerization of metal atoms on the neighbouring chains, suppression of the in-plane displacement on half of the chains may well lead to a suppression of the metal-metal pairing on the other half.

#### 4 Method of calculation

The calculations performed in this study are based on density functional theory (DFT) and the local density approximation (LDA) [73, 74]. As in our previous work on  $CrO_2$  [75, 76],  $MoO_2$  [23], and  $NbO_2$  [24] we employ the augmented spherical wave (ASW) method [77] in its scalar-relativistic implementation (see Refs. [78, 79, 80] for more recent descriptions). Since the ASW method uses the atomic sphere approximation (ASA) [81], we had to insert so-called empty spheres into the open crystal structures of  $VO_2$ . These empty spheres are pseudo atoms without a nucleus, which are used to model the correct shape of the crystal potential in large voids. In order to minimize the sphere overlap we have recently developed the sphere geometry optimization (SGO) method, which solves the problem of finding optimal empty sphere positions as well as radii of all spheres automatically [82]. The routine was applied to all three crystal structures under consideration. For the rutile structure, addition of 16 empty spheres allowed to keep the linear overlap of any pair of physical spheres below 15% and the overlap of any pair of physical and empty spheres below 20%. The positions of the

empty spheres are listed in Table 7. In addition to the empty sphere positions the

**Table 7** Empty sphere positions for the rutile structure.

Atom	Wyckoff positions	parameters		
		$x$	$y$	$z$
E <sub>1</sub>	(4c)			
E <sub>2</sub>	(4g)	0.3238	-0.3238	
E <sub>3</sub>	(16k)	0.0109	0.2973	0.2358

SGO algorithm proposed atomic sphere radii for all spheres, which are listed in Table 8 together with the orbitals used as the basis set for the present calculations. States

**Table 8** Atomic sphere radii and basis set orbitals used for the rutile structure.

Atom	Radius/ $a_B$	Orbitals			
V	2.230	4s	4p	3d	(4f)
O	1.831	2s	2p	(3d)	
E <sub>1</sub>	1.572	1s	(2p)		
E <sub>2</sub>	1.692	1s	2p	(3d)	
E <sub>3</sub>	0.949	1s	(2p)		

given in parentheses were included as tails of the other orbitals (see Refs. [77, 78, 80] for more details on the ASW method).

Applying the SGO algorithm to the monoclinic M<sub>1</sub> structure we were able, by inserting 48 empty spheres, to keep the linear overlap of any pair of physical spheres below 16%, and the overlap of any pair of physical and empty spheres below 21%. The positions of the empty spheres, the atomic sphere radii for all spheres as proposed by the SGO algorithm as well as the basis set orbitals are listed in Tables 9 and 10.

Finally, for the monoclinic M<sub>2</sub> structure, we were able, by inserting 29 empty spheres, to keep the linear overlap of any pair of physical spheres below 17%, and the overlap of any pair of physical and empty spheres below 22%. The positions of the empty spheres are listed in Table 11 and the corresponding atomic sphere radii as well as the basis set orbitals are given in Table 12.

Self-consistency was achieved by an efficient algorithm for convergence acceleration [83]. The Brillouin zone sampling was done using an increased number of  $\mathbf{k}$ -points ranging from 18 to 1800 points, 54 to 6750 points, and 63 to 1088 points, respectively, within the irreducible wedges of the three Brillouin zones. This way we were able to ensure convergence of our results with respect to the fineness of the  $\mathbf{k}$  space grid.

In addition to analyzing the band structure and the (partial) densities of states we will also address chemical bonding in terms of the crystal orbital overlap popula-

**Table 9** Empty sphere positions for the  $M_1$  structure.

Atom	Wyckoff positions	parameters		
		$x$	$y$	$z$
E <sub>1</sub>	(2d)	0.5	0.5	0.0
E <sub>2</sub>	(4e)	0.1346	-0.0037	0.4998
E <sub>3</sub>	(4e)	0.4026	0.1483	-0.2102
E <sub>4</sub>	(4e)	0.0833	-0.2432	0.1602
E <sub>5</sub>	(4e)	0.3274	0.2118	0.4983
E <sub>6</sub>	(4e)	0.2726	-0.1788	0.4289
E <sub>7</sub>	(4e)	0.0141	-0.0326	0.2357
E <sub>8</sub>	(4e)	0.2317	-0.0336	0.2812
E <sub>9</sub>	(4e)	0.1289	-0.0016	-0.2788
E <sub>10</sub>	(2b)	0.5	0.0	0.0
E <sub>11</sub>	(4e)	0.4375	0.1054	0.2706
E <sub>12</sub>	(4e)	0.1704	0.2552	0.0292
E <sub>13</sub>	(4e)	0.3768	-0.0322	-0.3779

**Table 10** Atomic sphere radii and basis set orbitals for the  $M_1$  structure.

Atom	Radius/ $a_B$	Orbitals			
V	2.042	4s	4p	3d	(4f)
O <sub>1</sub>	1.841	2s	2p	(3d)	
O <sub>2</sub>	1.739	2s	2p	(3d)	
E <sub>1</sub>	1.832	1s	2p	(3d)	
E <sub>2</sub>	1.753	1s	2p	(3d)	
E <sub>3</sub>	1.772	1s	2p	(3d)	
E <sub>4</sub>	1.734	1s	2p	(3d)	
E <sub>5</sub>	1.236	1s	(2p)		
E <sub>6</sub>	1.213	1s	(2p)		
E <sub>7</sub>	0.978	1s	(2p)		
E <sub>8</sub>	0.974	1s	(2p)		
E <sub>9</sub>	0.992	1s	(2p)		
E <sub>10</sub>	0.841	1s	(2p)		
E <sub>11</sub>	0.794	1s	(2p)		
E <sub>12</sub>	0.791	1s	(2p)		
E <sub>13</sub>	0.841	1s	(2p)		

**Table 11** Empty sphere positions for the M<sub>2</sub> structure.

Atom	Wyckoff positions	parameters		
		$x$	$y$	$z$
E <sub>1</sub>	(8j)	0.2491	0.1251	-0.0019
E <sub>2</sub>	(2c)	0.0	0.0	0.5
E <sub>3</sub>	(4h)	0.0	0.3149	0.5
E <sub>4</sub>	(4i)	0.0765	0.0	0.1518
E <sub>5</sub>	(8j)	0.1597	0.2525	-0.3270
E <sub>6</sub>	(4i)	0.3736	0.0	-0.1461
E <sub>7</sub>	(8j)	0.0075	0.1525	-0.2867
E <sub>8</sub>	(4i)	0.3932	0.0	-0.4322
E <sub>9</sub>	(4i)	0.2241	0.0	0.2109
E <sub>10</sub>	(4i)	0.4763	0.0	-0.3109
E <sub>11</sub>	(8j)	0.1604	0.2567	-0.0648

**Table 12** Atomic sphere radii and basis set orbitals for the M<sub>2</sub> structure.

Atom	Radius/ $a_B$	Orbitals			
V <sub>1</sub>	2.213	4s	4p	3d	(4f)
V <sub>2</sub>	2.085	4s	4p	3d	(4f)
O <sub>1</sub>	1.848	2s	2p	(3d)	
O <sub>2</sub>	1.817	2s	2p	(3d)	
O <sub>3</sub>	1.705	2s	2p	(3d)	
E <sub>1</sub>	1.642	1s	2p	(3d)	
E <sub>2</sub>	1.892	1s	2p	(3d)	
E <sub>3</sub>	1.978	1s	2p	(3d)	
E <sub>4</sub>	1.929	1s	2p	3d	(4f)
E <sub>5</sub>	1.795	1s	2p	(3d)	
E <sub>6</sub>	1.781	1s	2p	(3d)	
E <sub>7</sub>	1.104	1s	(2p)		
E <sub>8</sub>	1.195	1s	(2p)		
E <sub>9</sub>	1.143	1s	(2p)		
E <sub>10</sub>	0.892	1s	(2p)		
E <sub>11</sub>	0.868	1s	(2p)		

tion (COOP) as based on the notions introduced by Hoffmann [84] as well as related concepts. Among the latter are the crystal orbital Hamiltonian population (COHP) as proposed by Dronskowski and Blöchl [87] and the covalence energy by Börnsen *et al.* [88, 89]. All these quantities have been implemented in the ASW method [85] (see

also Refs. [16, 86]) and have been validated for a large number of compounds [16].

## 5 Results for metallic VO<sub>2</sub>

### 5.1 Molecular orbital picture

Our expectations on the electronic structure of VO<sub>2</sub> are easily stated within the molecular orbital picture proposed by Goodenough (see Sec. 2.2) [3, 6, 7]. The general situation is visualized in Fig. 8. First, hybridization between the oxygen 2*p* and vanadium

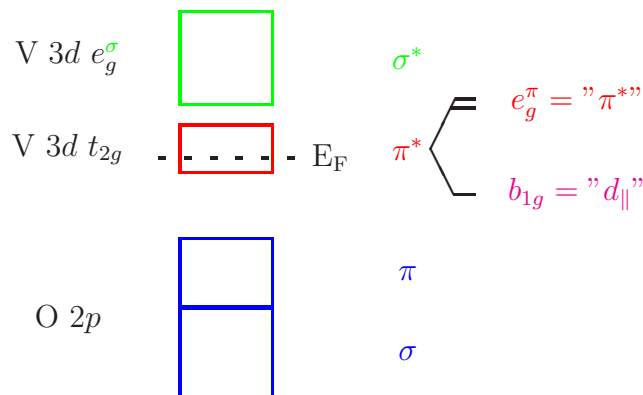


**Fig. 8** Molecular orbital scheme for rutile VO<sub>2</sub>.

3*d* orbitals will lead to  $\sigma$ - and  $\pi$ -type overlap. This gives rise to states of  $\sigma$  and  $\sigma^*$  as well as  $\pi$  and  $\pi^*$  character. Since the  $p$ - $d$  overlap is stronger for the former these states experience the larger bonding-antibonding splitting. While the  $\sigma$  and  $\pi$  states will be filled and primarily of O 2*p* character, the corresponding antibonding bands will be dominated by the V 3*d* orbitals. Due to the electron count, the latter will be found at and above the Fermi energy. In the nearly perfect cubic octahedral surrounding of the vanadium atoms, the  $\sigma^*$  and  $\pi^*$  states are of  $e_g^\sigma$  and  $t_{2g}$  symmetry, respectively. We identify these orbitals in Fig. 5 as the  $d_{3z^2-r^2}/d_{xy}$  and the  $d_{x^2-y^2}/d_{xz}/d_{yz}$  orbitals, respectively. Note that the albeit small orthorhombic distortions of the oxygen octahedra lift all the degeneracies among the  $d$  orbitals. As already pointed out by Goodenough, the exact position and width of the  $d$  bands is subject not only to the  $p$ - $d$  hybridization but also strongly influenced by direct metal-metal interactions [3, 6]. In particular, in the rutile structure such interactions involve the  $d_{x^2-y^2}$  orbitals, which experience strong overlap parallel to the rutile  $c$  axis. These orbitals are of  $b_{1g}$  symmetry but are usually designated as the  $d_{\parallel}$  bands. The remaining  $t_{2g}$  orbitals are of  $e_g^\pi$  symmetry and usually subsumed under the name  $\pi^*$  (not to be mixed with the same notation used above for the  $t_{2g}$  states as a whole). While the  $d_{xz}$  orbitals experience hardly any overlap with orbitals of neighbouring metal atoms the  $d_{yz}$  states mediate

metal-metal bonding parallel to the in-plane axes of the tetragonal cell. The general situation was already sketched in Fig. 2.

The validity of the just outlined general band scheme for the rutile-type transition-metal dioxides has been already confirmed in our previous calculations for hypothetical rutile MoO<sub>2</sub> as well as metallic NbO<sub>2</sub> [23, 24]. Furthermore, from the close relationship of the crystal structures of all three compounds we expect a very similar electronic structure also for VO<sub>2</sub>. Yet, as compared to the 4*d* systems the vanadium *d* bands will display smaller bandwidths.

### 5.2 Band structure and density of states

We display in Fig. 9 the electronic states along selected high symmetry lines within

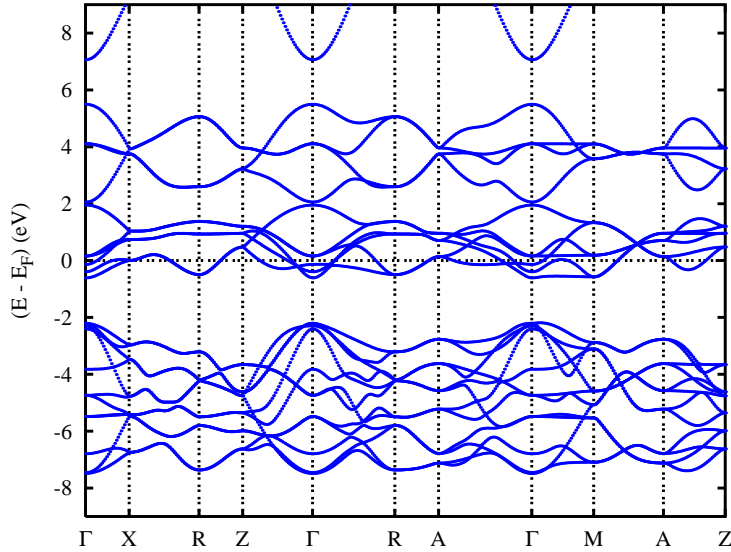


**Fig. 9** Electronic bands of rutile VO<sub>2</sub> along selected symmetry lines within the first Brillouin zone of the simple tetragonal lattice, Fig. 10(a).

the first Brillouin zone of the simple tetragonal lattice, Fig. 10(a). The corresponding partial densities of states (DOS) are given in Fig. 11. The total density of states at the Fermi energy,  $N(E_F)$ , is 2.63 states/f.u./eV. Not shown are low lying oxygen 2*s* states.

In Figs. 9 and 11 we identify four groups of bands. In the energy range from -7.6 to -2.2 eV we observe 12 bands, which trace back mainly to O 2*p* states but have a non-negligible contribution due to the V 3*d* states. Bands are most easily counted along the direction X-R where they are twofold degenerate. The next two groups, which extend from -0.6 to 2.0 eV and from 2.0 to 5.5 eV, contain six and four bands, respectively. They originate mainly from V 3*d* states. Yet, *p-d* hybridization causes additional O 2*p* contributions in this energy range. From the above molecular-orbital point of view we interpret the bands between -7.6 and -2.2 eV as the O 2*p*-dominated

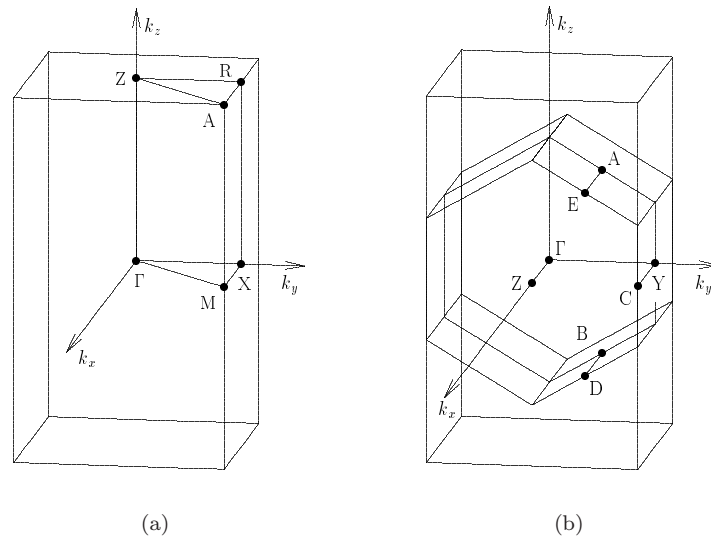


**Fig. 10** First Brillouin zones of the (a) simple tetragonal and (b) simple monoclinic lattices. Backfolding of the tetragonal Brillouin zone implies the following transformation of high symmetry points:  $X_T \rightarrow Y_M, Z_M$ ;  $M_T \rightarrow C_M$ ;  $Z_T \rightarrow Y_M$ ;  $R_T \rightarrow \Gamma$ ;  $A_T \rightarrow Z_M$ .

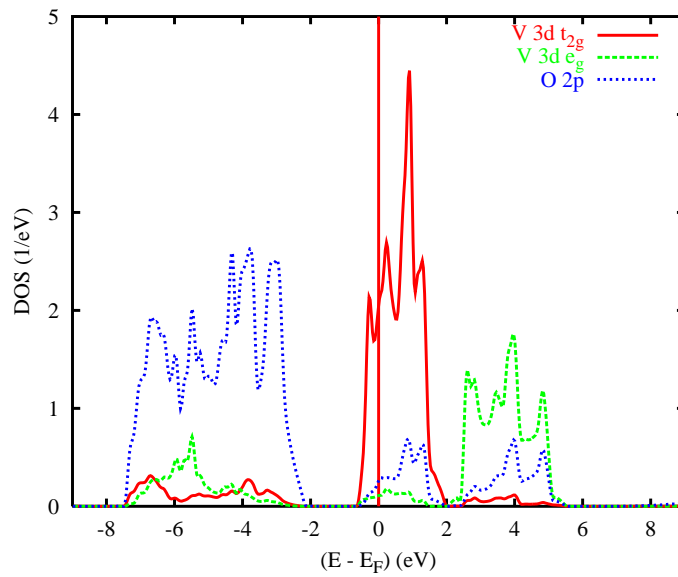


**Fig. 11** Partial densities of states (DOS) of rutile  $\text{VO}_2$  per formula unit.

lower  $\sigma$  and higher  $\pi$  states. The respective  $\pi^*$  and  $\sigma^*$  states are found in the energy intervals from -0.6 to 2.0 eV and 2.0 to 5.5 eV. Finally, we observe V 4s states starting at 7.0 eV.

Crystal field splitting expected from the fact that the metal atoms are located at the centers of slightly distorted VO<sub>6</sub> octahedra is observed in the partial V 3d DOS shown in Fig. 12. There we have included only the single vanadium atom at the corner

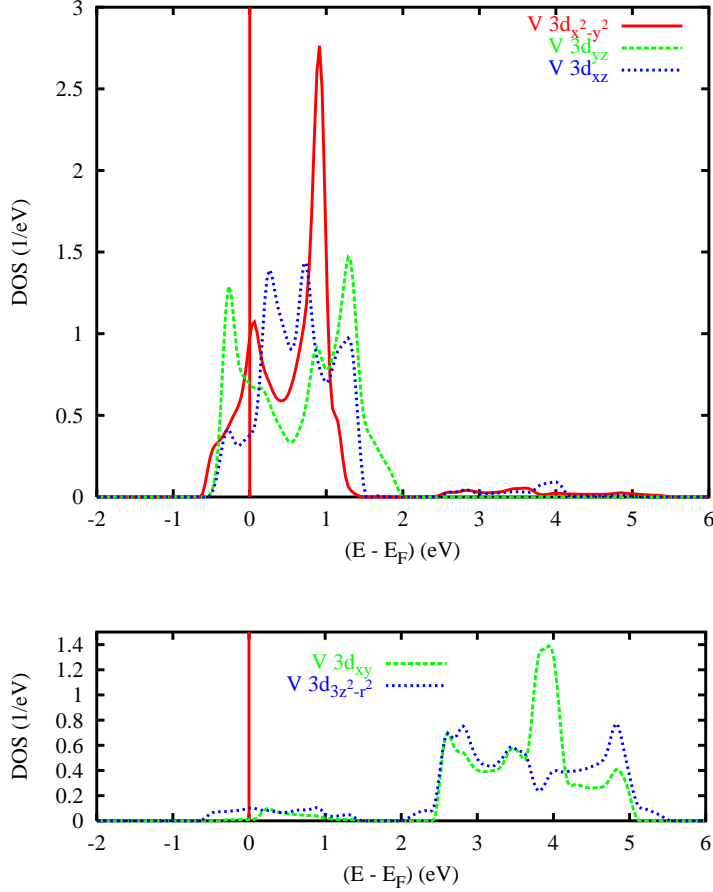


**Fig. 12** Partial V 3d  $t_{2g}$  and  $e_g$  densities of states (DOS) of rutile VO<sub>2</sub>. Selection of orbitals is relative to the local rotated reference frame.

of the rutile cell and used the local rotated reference frame introduced in Sec. 3.1. Fig. 12 clearly reveals the almost perfect energetical separation of the 3d  $t_{2g}$  and  $e_g$  groups of bands. The former states appear almost exclusively in the energy range from -0.6 to 2.0 eV. The  $e_g$  states dominate the bands between 2.0 and 5.5 eV. The small but finite  $t_{2g}$ - $e_g$  configuration mixing is a measure of octahedral distortions. Contributions of the V 3d states to the oxygen bands are slightly larger for the  $e_g$  states which, forming  $\sigma$  bonds, experience a larger overlap with the O 2p states. For the same reason, the bonding-antibonding splitting is larger for the  $e_g$  states as compared to the  $t_{2g}$  states,

which give rise to  $\pi$  bonds.

In Fig. 12 the differences between the single symmetry components of the  $t_{2g}$  and  $e_g$  orbitals, respectively, reflect the orthorhombic site symmetry. Worth mentioning is the pronounced double peak structure of the  $d_{yz}$  partial DOS. Since the respective orbitals point along the two in-plane  $a$  axes of the tetragonal cell these double maxima result from metal-metal bonding. Finally, the  $d_{x^2-y^2}$  partial DOS displays an albeit smaller separation into two peaks, which is due to the overlap of these orbitals parallel to the rutile  $c$  axis.

Our findings are in perfect accordance with the molecular orbital picture proposed by Goodenough [6, 7], which was sketched in Sec. 5.1. There the  $d_{x^2-y^2}$  states were designated as the  $d_{\parallel}$  states and the notation  $\pi^*$  was used for the  $d_{xz}$  and  $d_{yz}$  states. Deviations from the band diagram of Goodenough show up with respect to the widths of the different bands. Goodenough and many authors after him assumed the  $d_{\parallel}$  band to be considerably more narrow than the  $\pi^*$  bands. Yet, our calculation reveals similar widths of all three  $t_{2g}$  bands. In particular the  $d_{\parallel}$  band has a width of  $\approx 1.5$  eV. Of course, this has strong implications for model approaches building on strong correlations within this band.

While the results for rutile  $\text{VO}_2$  agree very well with those for hypothetical rutile  $\text{MoO}_2$  [23] differences appear in a more detailed analysis of the single symmetry components of the  $t_{2g}$  orbitals as given in Fig. 12. In  $\text{MoO}_2$ , the Mo  $4d_{x^2-y^2}$  band shows a strong tendency towards bonding-antibonding splitting while the remaining  $t_{2g}$  bands give rise to very similar densities of states. In contrast, in  $\text{VO}_2$  bonding-antibonding splitting of the V  $3d_{x^2-y^2}$  band is much weaker. At the same time, the  $3d_{xz}$  and  $3d_{yz}$  partial DOS show distinct deviations. In particular, the latter reveals some splitting into two peaks at about -0.3 and 1.3 eV. These features may be traced back to the much larger  $c$  axis of  $\text{VO}_2$  (2.8514 Å vs. 2.805 Å in  $\text{MoO}_2$ ), which leads to a larger separation of the metal atoms along this axis. In contrast, the rutile  $a$  axis is reduced (4.5546 Å vs. 4.856 Å in  $\text{MoO}_2$ ). This causes a larger overlap of metal  $d$  orbitals within the planes and, hence, a visible bonding-antibonding splitting of the local  $d_{yz}$  orbitals.

Whereas our calculations are in good agreement with the calculations by Caruthers *et al.* as well as by Gupta *et al.* [55, 56], a closer look reveals small but distinct deviations concerning the exact band positions and, consequently, the Fermi surface. We attribute these differences to the approximations inherent in the old calculations. Good agreement, however, is found in a comparison with the existing state-of-the-art calculations by Wentzcovitch *et al.* [8] as well as Kurmaev *et al.* [59]. Minor differences in the band structures may result from the use of the crystal structure data of Ref. [71] or from Brillouin zone samplings with different numbers of  $\mathbf{k}$ -points. Finally, we observe distinct deviations in the recent calculations by Nikolaev *et al.* with respect to the band positions [57]. While our calculations give an occupied V  $3d$  bandwidth of 0.6 eV, in close agreement with Wentzcovitch *et al.*, Nikolaev *et al.* report a value of 0.77 eV. At the same time, the latter authors locate the upper edge of the O  $2p$  bands 1.39 eV below the Fermi level. In our calculation the band maximum is found at -2.4 eV in almost perfect agreement with both the optical measurements by Verleur *et al.* and the photoemission data by Powell *et al.*, Shin *et al.*, Bermudez *et al.* as well as Goering *et al.*. These authors find the O  $2p$  states 2.4-2.5 eV below the Fermi energy [39, 40, 41, 42, 43, 45]. The total width of the O  $2p$  band of 5.37 eV reported

by Nikolaev *et al.* is again in agreement with our value of  $\approx 5.6$  eV. Finally, we point to the almost equal densities of states at the Fermi energy of all three  $t_{2g}$  orbitals, which confirm the reported isotropic conductivity [49, 50].

### 5.3 Chemical bonding

Chemical bonding is addressed via the covalence energy shown in Fig. 13. The curves

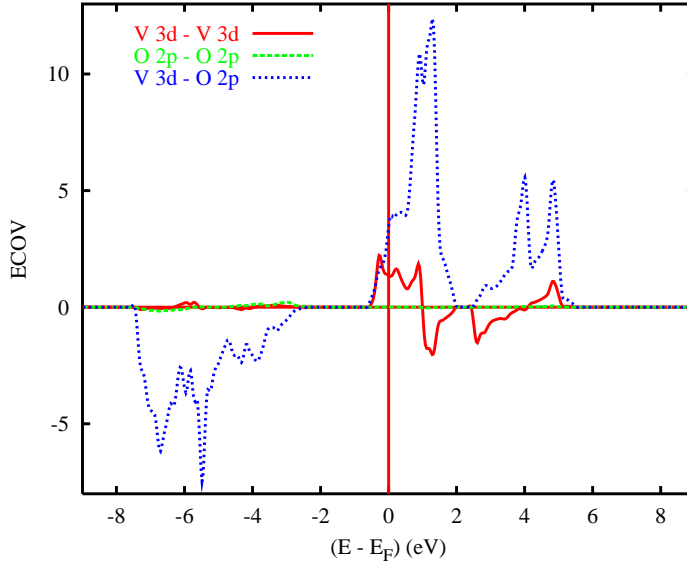


**Fig. 13** Partial covalence energies ( $E_{cov}$ ) of rutile VO<sub>2</sub>.

display the “canonical” behaviour being negative (bonding) and positive (antibonding) in the low and high energy regions. While the oxygen-oxygen overlap is almost negligible we observe considerable metal-metal bonding in the V 3d dominated groups of bands. Obviously, the dominating contribution to the total bonding results from the V 3d–O 2p bonding. Below  $E_F$ , the corresponding  $E_{cov}$  curve is negative below  $-2.2$  eV and positive only in the small energy range of the occupied V 3d derived bands.

### 5.4 Comparison to experiment

We display in Figs. 14 and 15 total and partial V 3d and O 2p densities of states folded with a Gaussian of 0.25 and 0.5 eV width, respectively, for the occupied and unoccupied part of the spectrum. In Fig. 14 we have added UPS spectra as measured by Goering *et al.* [43, 45]. Good agreement of the calculated and measured curves is found. In addition, the calculated total DOS compares very well with the XPS and UPS spectra by Blaauw *et al.*, Shin *et al.* and Bermudez *et al.* [46, 41, 42]. The occupied bandwidth of  $\approx 8.5$  eV deduced from the experiments is close to the calculated 8.0 eV. According to the XPS and UPS spectra the valence band is split into a low and high binding part of about 1.5 and 6 eV width, respectively [46, 41, 45]. Whereas the low binding

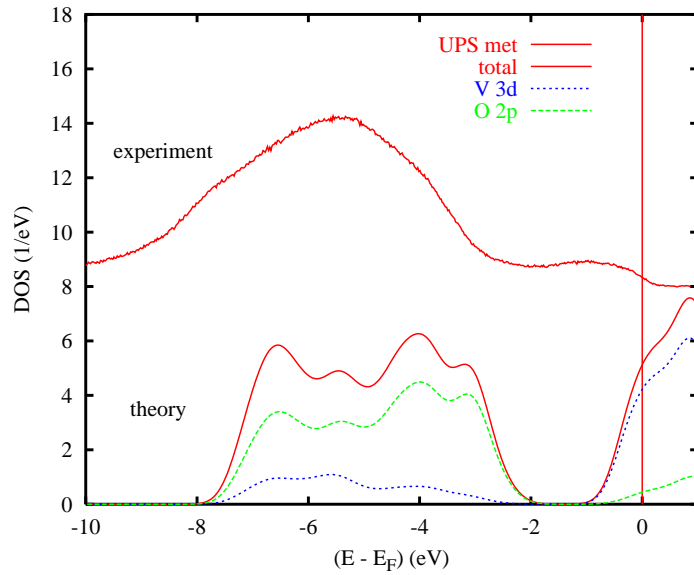


**Fig. 14** Total and partial densities of states (DOS) of rutile  $\text{VO}_2$  folded with a 0.25 eV wide Gaussian (lower set of curves) and UPS spectra (upper curve; note the offset introduced in order to distinguish experimental and theoretical results; from Ref. [43, 45]).

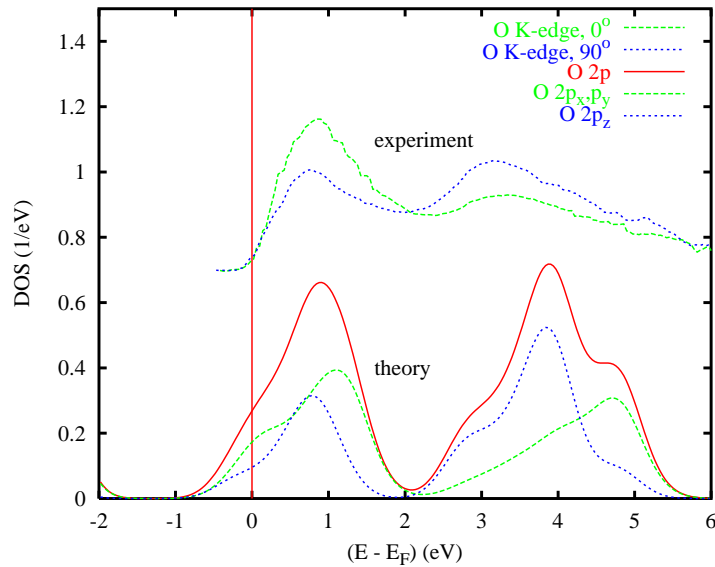


**Fig. 15** Partial  $\text{O } 2p$  densities of states (DOS) of rutile  $\text{VO}_2$  folded with a 0.5 eV wide Gaussian (lower set of curves) and XAS  $\text{O K}$  edge spectra (upper set of curves; note the offset introduced in order to distinguish experimental and theoretical results; from Ref. [90, 48]; data shifted by 529.5 eV).

region results from a single peak centered at  $\approx -1.0$  eV, which is attributed to the V  $3d$  states, the high binding region, resulting mainly from the O  $2p$  states, is dominated by a large peak at  $\approx -5.5$  eV and shows two slight shoulders at -4.0 and -7.5 eV [43, 45]. In contrast, as compared to the UPS data, the XPS spectra display a considerably higher intensity at energies below -5.5 eV and a strong decrease in intensity around the top of the O  $2p$  band [46, 41]. Since the V  $3d$  states have a larger cross section in XPS [91] this shift of intensity reveals a considerable V  $3d$  contribution especially to the bands below -5.5 eV and, hence, a strong  $p$ - $d$  hybridization in this energy region. This is well reflected by the calculations.

In Fig. 15 we have complemented the theoretical results by soft-X-ray absorption spectra as measured by Müller *et al.* [90, 48]. The experimental data are shifted by 529.5 eV. In order to probe the angular dependence, in these experiments the polarization vector  $\mathbf{E}$  was oriented either parallel ( $\phi = 90^\circ$ ) or else perpendicular ( $\phi = 0^\circ$ ) to the rutile  $c$  axis. In the former case, dipole selection rules allow for transitions from O  $1s$  to the O  $2p_z$  state. In contrast, for  $\mathbf{E}$  perpendicular to the  $c$  axis transitions to the O  $2p_x$  and  $2p_y$  states may occur. The curves given by Müller conform with the spectra by Abbate *et al.* who found, for metallic VO<sub>2</sub>, two peaks at 529.9 and 532.5 eV photon energy for  $\mathbf{E} \parallel c$  [47]. In the spectra given by Müller *et al.* these peaks are located at 530.3 and 532.7 eV, respectively [48]. However, as Müller has pointed out previously, the curves actually can be fitted to four peaks at 530.1, 530.7, 532.7, and 534.7 eV [90]. In the energy-shifted spectra of Fig. 15 these peaks are located at 0.6, 1.2, 3.2, and 5.2 eV.

In Fig. 15, the partial DOS correspond to the final states, which are occupied in the XAS experiments. Note that the curve marked O  $2p_x, p_y$  comprises only the mean average of these orbitals since the component perpendicular to  $\mathbf{E}$  is not seen in experiment. For the same reason, the curve marked O  $2p$  actually contains the full contribution from the  $p_z$  orbital but only half of the contributions from the  $p_x$  and  $p_y$  orbitals. As for the occupied part of the spectrum we observe overall good agreement between experiment and theory. This holds for the positions of the peaks, their relative intensity and their angular dependence. Still, agreement seems to be less satisfactory in the high energy region between 4 and 5 eV. However, the discrepancy is resolved by the aforementioned four peak analysis of the experimental spectra. Finally, differences with respect to intensities may be attributed to matrix element and core-hole effects, which might be important but are not accounted for in our present analysis [92, 47].

### 5.5 Fermi surface

Despite the good agreement of our results with previous experimental and calculated data we are still seeking for more conclusive arguments for the destabilization of the rutile structure of VO<sub>2</sub> at low temperatures. Since the metal-insulator transition is accompanied by a structural transformation one might be tempted to deduce more information about the origin of the transition from investigating the Fermi surface. This has been already done by Gupta *et al.* in the course of their non-selfconsistent calculations [56]. Furthermore, investigation of the Fermi surface of hypothetical rutile MoO<sub>2</sub> in our previous work revealed strong nesting on flat portions at height  $q_z = \pm \frac{\pi}{2c}$ . This indicated a possible splitting of the  $d_{x^2-y^2}$ , which was indeed observed in

monoclinic MoO<sub>2</sub> [23].

Cuts through the Fermi surface parallel to the {100} and {110} planes as resulting from the present calculations are shown in Figs. 16, 17, and 18. They contain the  $\Gamma$ -X-

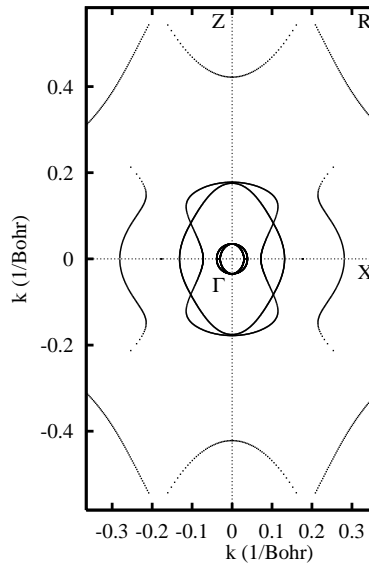


**Fig. 16** {100} cut through the Fermi surface of rutile VO<sub>2</sub>.

Z-R,  $\Gamma$ -M-Z-A, and X-M-R-A planes, which are the vertical borders of the irreducible wedge of the first Brillouin zone, Fig. 10(a). As before, interpretation of the figures is greatly facilitated by combining them with the band structure shown in Fig. 9. We recognize electron- and hole-like regions near the  $\Gamma$ - and Z-point, respectively. Nevertheless, in contrast to the non-selfconsistent calculations by Gupta *et al.*, our calculations do not allow to identify any Fermi surface nesting in Figs. 16 to 18, which might be indicative of a destabilization of the rutile structure. This is in contrast to the aforementioned findings for hypothetical rutile MoO<sub>2</sub>. However, since VO<sub>2</sub> has one *d* electron less, the differences between both compounds were to be expected. We thus conclude, that investigation of the Fermi surface does not allow for an explanation of the instability of the rutile structure. In so far, our result resembles the above mentioned argument of Goodenough against a Jahn-Teller-type distortion as the major source for the crystal structure deformations.

### 5.6 Symmetry analysis of the band structure

In order to find a common origin of the instability of the rutile structure in the  $d^1$ ,  $d^2$ , and  $d^3$  transition-metal dioxides we proceed along the same lines as in our work on MoO<sub>2</sub> and NbO<sub>2</sub> and perform a detailed analysis of the electronic states. To this end we display in Figs. 19, 20, and 21 the electronic bands in the narrow energy range from -1.0 to 2.5 eV about the Fermi energy in the same special representation as in

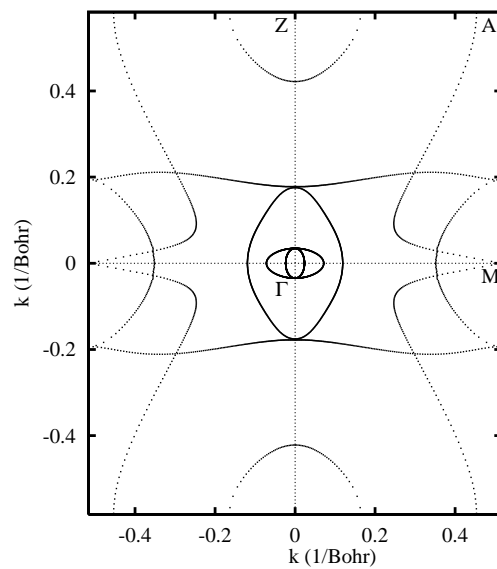


Fig. 17  $\{110\}$  cut through the Fermi surface of rutile VO<sub>2</sub>.

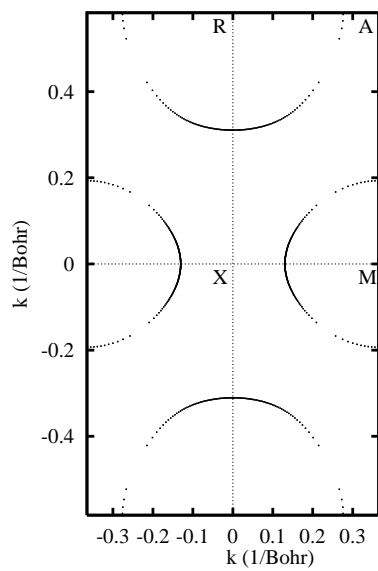
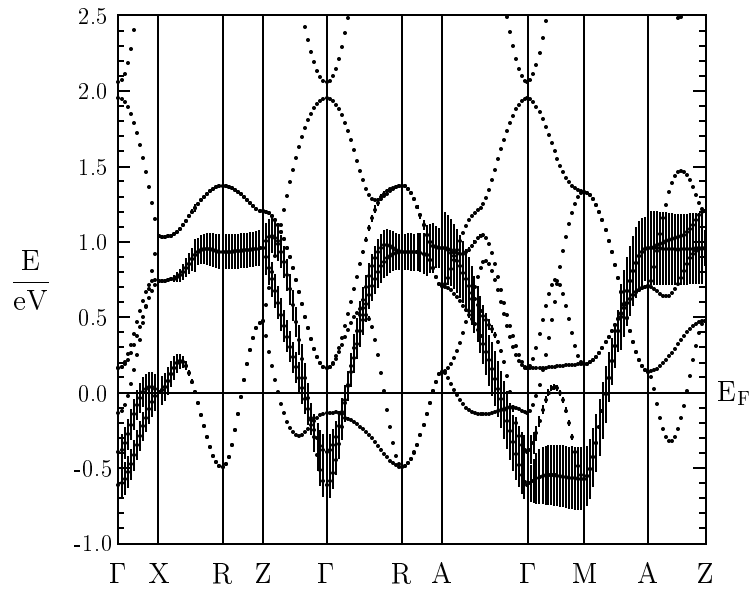
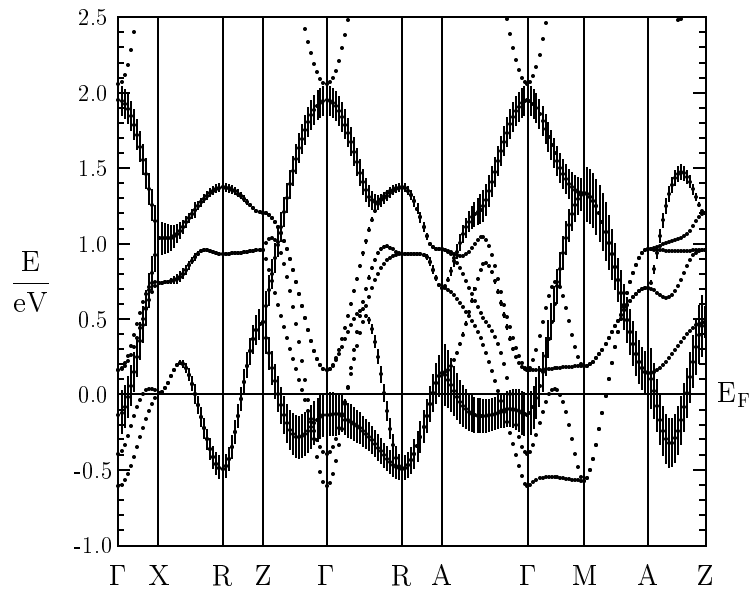


Fig. 18  $\{100\}$  cut through the Fermi surface of rutile VO<sub>2</sub>.



**Fig. 19** Weighted electronic bands of rutile  $\text{VO}_2$ . The width of the bars given for each band indicates the contribution due to the  $3d_{x^2-y^2}$  orbital of the V atom at  $(0,0,0)$  relative to the local rotated reference frame.



**Fig. 20** Weighted electronic bands of rutile  $\text{VO}_2$ . The width of the bars given for each band indicates the contribution due to the  $3d_{yz}$  orbital of the V atom at  $(0,0,0)$  relative to the local rotated reference frame.

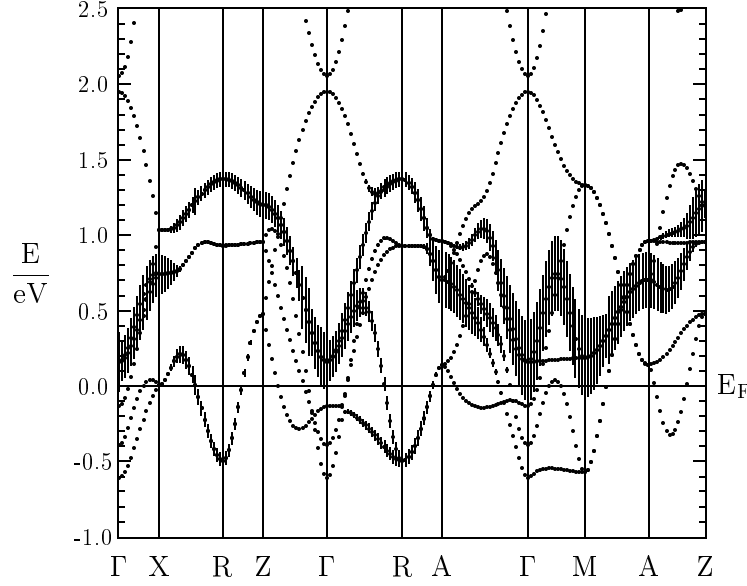


**Fig. 21** Weighted electronic bands of rutile VO<sub>2</sub>. The width of the bars given for each band indicates the contribution due to the  $3d_{xz}$  orbital of the V atom at (0,0,0) relative to the local rotated reference frame.

our work on MoO<sub>2</sub> [23]: In all three figures, each band at each  $\mathbf{k}$ -point is given a bar, which length is a measure for the contribution from a specified orbital. Since we again refer to the local frame of reference, Figs. 19 to 21 correspond to the partial V  $3d t_{2g}$  DOS shown in Fig. 12, which likewise made use of the local coordinate system.

As in MoO<sub>2</sub> and NbO<sub>2</sub> we observe in Fig. 19 a strong dispersion of the metal  $3d_{x^2-y^2}$  derived bands along all lines parallel to  $\Gamma$ -Z. In contrast, the dispersion perpendicular to this line is almost negligible. Again, we attribute this dispersion to the overlap of  $d_{x^2-y^2}$  orbitals at metal sites neighbouring in  $z$  direction. As compared to MoO<sub>2</sub> the width of these bands relative to the total  $t_{2g}$  band width is reduced. This is due to the increased value of the rutile  $c$  axis and, hence, the larger metal-metal distance in this direction. In contrast, the smaller value of the  $a$  axis in VO<sub>2</sub> causes a larger interchain interaction. This leads to an increased splitting of the  $d_{x^2-y^2}$  bands along the lines  $\Gamma$ -M and A-Z as well as along the lines where the strong dispersion is observed.

The V  $3d_{yz}$  derived bands are highlighted in Fig. 20. They show a large dispersion in all directions and, as in MoO<sub>2</sub>, a large splitting at the  $\Gamma$ -point. The latter is a consequence of the underlying body-centered tetragonal lattice formed by the metal atoms and results from backfolding the bands from the Brillouin zone of this lattice to the smaller one of the simple tetragonal lattice. This effect can be read off from the bands along the lines connecting the  $\Gamma$ -point to the X-, M-, A-, and Z-point, respectively.

Finally, the V  $3d_{xz}$  derived bands display the smallest dispersion. This is due to

the fact that these orbitals induce no substantial  $\sigma$ -type overlap with neighbouring metal atoms. Instead, they mediate the small coupling between the octahedral chains. Still, the larger width of these bands as compared to MoO<sub>2</sub> results from the increased interchain coupling coming with the smaller value of the  $a$  lattice constant.

Of course, the previous analysis of the  $t_{2g}$  bands with its nearly unique assignment of a single character to each band as well as the subsequent interpretation in terms of the geometric coordination of the atoms and their orbitals benefitted from the very small mixing among these states. Exceptions are the hybridization of the  $d_{x^2-y^2}$  bands with the  $d_{yz}$ - and  $d_{xz}$ -derived bands along the symmetry line X-R and, to a lesser degree, along the line  $\Gamma$ -A. Nevertheless, we point out that the three  $t_{2g}$  bands disperse almost completely independently and are coupled mainly via charge conservation. For this reason the  $d_{\parallel}$  band may be regarded as a one-dimensional band in a three-dimensional embedding background of  $\pi^*$  bands. The situation is thus identical to that found in rutile NbO<sub>2</sub> as well as in hypothetical rutile MoO<sub>2</sub> [23, 24]

Eventually, the finding of an only weak hybridization of the different types of bands has a strong impact on our further understanding since it will allow to establish a relation between particular atomic displacements and the response of the electronic states. This way, we may find a route to an understanding of the mechanisms leading to the low-temperature monoclinic structure.

## 6 Results for insulating M<sub>1</sub>-VO<sub>2</sub>

### 6.1 Band structure and density of states

The electronic bands of monoclinic VO<sub>2</sub> in the energy range of the V  $3d$  states are displayed in Fig. 22 along selected high symmetry lines within the simple monoclinic Brillouin zone, Fig. 10(b). The dominant partial densities of states (DOS) are given in Fig. 23. As before low lying oxygen  $2s$  states are not included.

In Figs. 22 and 23 we identify the same groups of bands as for rutile VO<sub>2</sub>. They comprise 24 oxygen  $2p$  dominated bands well below the Fermi level and two groups of 12 and 8 bands, respectively, at and above  $E_F$ . These latter two groups trace back mainly to V  $3d$  states. Finally,  $p$ - $d$  hybridization leads to V  $3d$  and O  $2p$  contributions of the order of about 10% in the energy regions where the respective other partner dominates. The energetical separation between the O  $2p$  and V  $3d$  derived bands turns out to be slightly smaller than in the rutile phase. This is in agreement with the XPS results by Blaauw *et al.* [46]. Again, these general findings conform well with the molecular orbital picture drawn in Sec. 5.1.

Nevertheless, on going into more detail we find distinct differences between the results for the rutile and the monoclinic structure. In particular, we witness the evolution of a sharp peaks in the V  $3d$   $t_{2g}$  partial DOS just below  $E_F$  and at  $\approx 1.3$  eV. In general, spectral weight is shifted from the central region of this group of bands to the edges. As a consequence, the density of states at the Fermi energy is lowered as compared to the rutile value and amounts to 2.08 states/f.u./eV.

In order to understand these differences we proceed displaying in Fig. 24 the single symmetry components of the V  $3d$  partial DOS. In doing so we include only the single

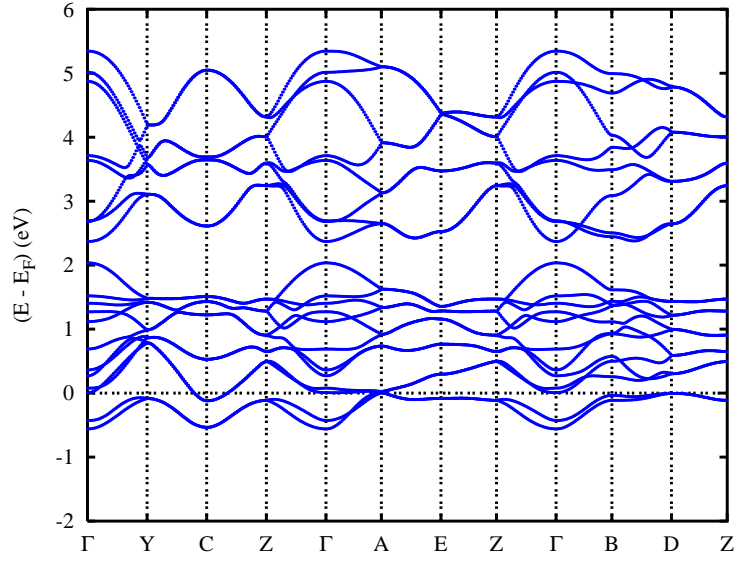


**Fig. 22** Electronic bands of monoclinic VO<sub>2</sub> along selected symmetry lines within the simple monoclinic Brillouin zone, Fig. 10(b).

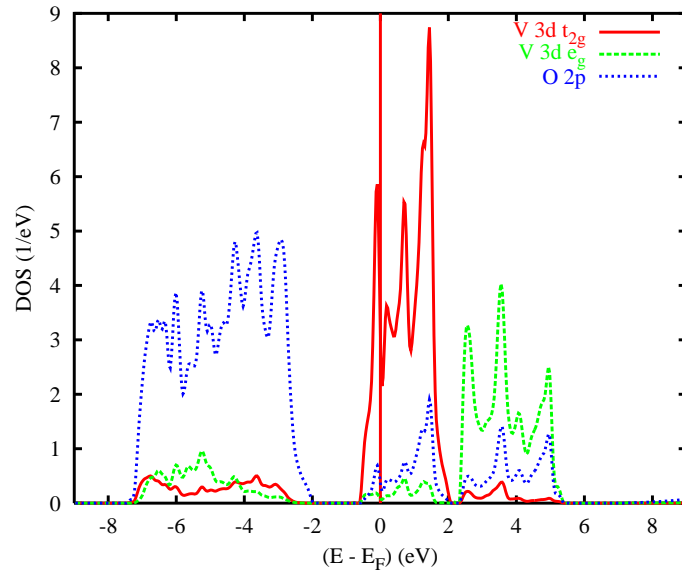


**Fig. 23** Partial densities of states (DOS) of monoclinic VO<sub>2</sub> per unit cell.

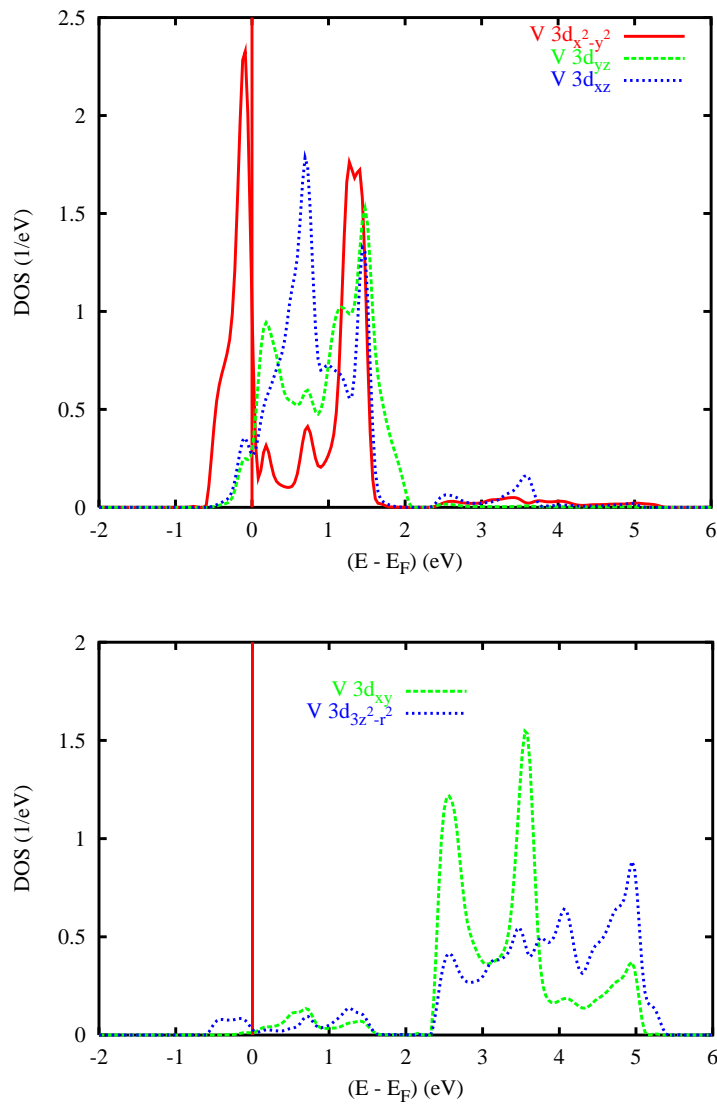


**Fig. 24** Partial V 3d  $t_{2g}$  and  $e_g$  densities of states (DOS) of monoclinic VO<sub>2</sub>. Selection of orbitals is relative to the local rotated reference frame.

vanadium atom near the corner of the underlying rutile cell and use the local rotated reference frame as defined in Sec. 3.1. As in Fig. 23 we recognize the almost perfect energetical separation of the  $3d$   $t_{2g}$  and  $e_g$  groups of bands, which results from the octahedral crystal field splitting. The small  $t_{2g}$ - $e_g$  configuration mixing again points to the slight distortions of the octahedra.

Concentrating on the  $t_{2g}$  partial DOS, we find close similarities of the  $d_{xz}$  and  $d_{yz}$  partial DOS to those calculated for the rutile structure given in Fig. 12. Yet, both bands have experienced a considerable energetical upshift and are left almost unoccupied.

While the  $d_{xz}$  and  $d_{yz}$  partial DOS still resemble each other the  $d_{x^2-y^2}$  partial DOS display striking deviations from both these two curves and the results obtained for the rutile structure. Comparing Fig. 12 to Fig. 24 we recognize strong splitting of the  $d_{x^2-y^2}$  partial DOS into two peaks, which are located just below  $E_F$  and at  $\approx 1.3$  eV. In addition, the partial DOS in between is considerably reduced. This leads to the decrease of the density of states at the Fermi energy.

Our findings for the  $t_{2g}$  states of monoclinic VO<sub>2</sub> are in good agreement with the band scheme proposed by Goodenough [6], which we sketched in Fig. 2. We thus attribute the striking behaviour of the  $d_{x^2-y^2}$  (or  $d_{\parallel}$ ) bands to the pairing of the vanadium atoms along the rutile  $c$  axis and the resulting bonding-antibonding splitting. In contrast, the energetical upshift of the  $d_{xz}$  and  $d_{yz}$  (or  $\pi^*$ ) bands results from the lateral antiferroelectric displacement of the vanadium atoms, which increases the  $p$ - $d$  bonding.

The situation becomes clearer from a comparison to the band structure of rutile VO<sub>2</sub> shown in Fig. 25. Here we have used the first Brillouin zone of the simple

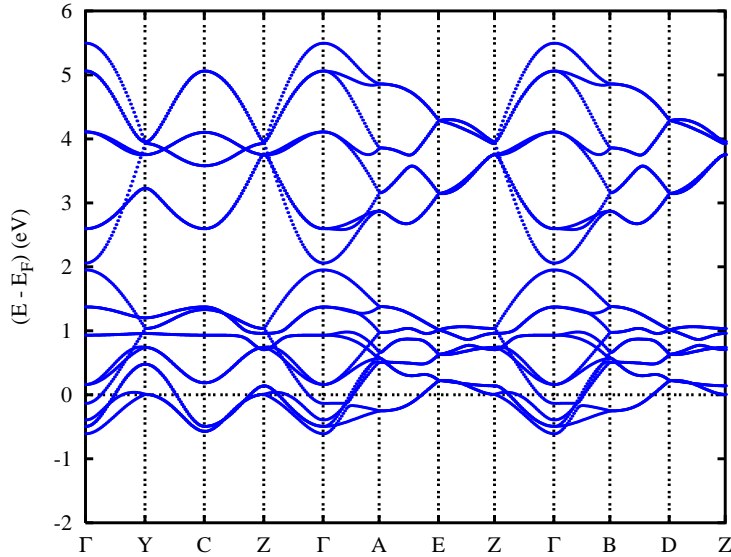


**Fig. 25** Electronic bands of rutile VO<sub>2</sub> along selected symmetry lines within the simple monoclinic Brillouin zone, Fig. 10(b).

monoclinic lattice, Fig. 10(b) and folded back all bands from the larger Brillouin zone of the tetragonal lattice, Fig. 10(a). Just in the same manner as for  $\text{MoO}_2$ , those two bands in Fig. 25, which give rise to the lowest states within the  $t_{2g}$ -derived group of bands at the  $\Gamma$ -point, bend upwards along the line  $\Gamma$ -A and cross the higher lying bands. In monoclinic  $\text{VO}_2$  these two bands are separated from the other states and form a split-off doublet, which, however, is still touching the higher lying bands at the A-point. For this reason, we end up with a finite density of states at the Fermi energy, which spoils the experimental finding of an insulating ground state with an optical band gap of about 0.6 eV. Instead, from the touching bands at the A-point and the occupied band width of the conduction band at the C-point of about 0.1 eV we would rather regard monoclinic  $\text{VO}_2$  as a semimetal, in agreement with the results by Wentzcovitch *et al.* [8]. Like these authors we attribute this failure of the calculations to the shortcomings of the local density approximation, which usually underestimates the band gap by about 50% and in some small gap semiconductors like Ge misses the gap at all. This seems to be also the case for monoclinic  $\text{VO}_2$ . Like in the zincblende-type semiconductors the optical band gap originates to a large part from bonding-antibonding splitting of hybridized bands, which, obviously, is not well enough accounted for by the LDA.

## 6.2 Chemical bonding

Again we investigate the chemical bonding by determining the covalence energy. The result is shown in Fig. 26. The  $E_{cov}$  curves for the O  $2p$ -O  $2p$  and the V  $3d$ -O

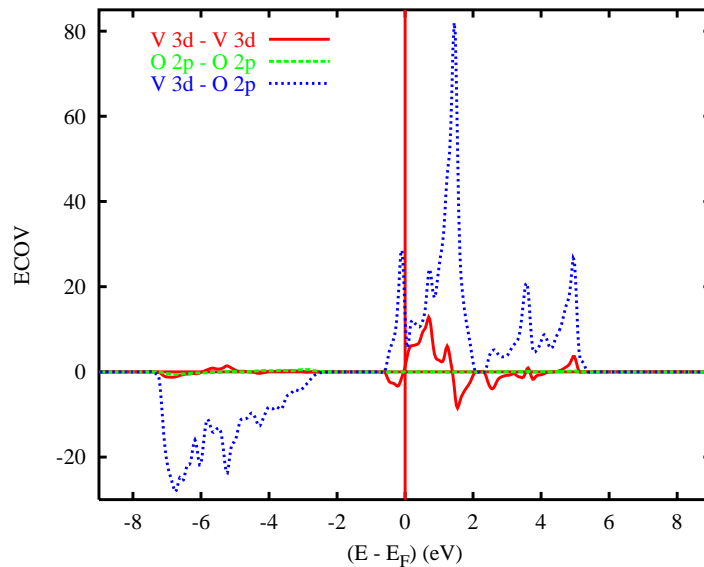


**Fig. 26** Partial covalence energies ( $E_{cov}$ ) of monoclinic  $\text{VO}_2$ .

$2p$  bonding agree fairly well with the respective curves for rutile  $\text{VO}_2$  as shown in Fig. 13. Qualitative differences show up in the V  $3d$ -V  $3d$  bonding. In particular,

we observe a change in sign in the energy region of the bonding V  $3d_{x^2-y^2}$  bands. While the respective  $E_{cov}$  curve in the lower half of the V  $3d$   $t_{2g}$  bands was positive (antibonding) for rutile VO<sub>2</sub> it has become negative (bonding) just below the Fermi energy in the M<sub>1</sub> structure. As for monoclinic MoO<sub>2</sub> this signals the increased metal-metal bonding due to the pairing of the metal atoms. Furthermore, the formation of bonding and antibonding V  $3d_{x^2-y^2}$  states below and above the Fermi energy, respectively, decreases the value of the total integrated  $E_{cov}$  at the Fermi level.

### 6.3 Comparison to experiment

As for metallic VO<sub>2</sub> we display in Figs. 27 and 28 total and partial V  $3d$  and O  $2p$

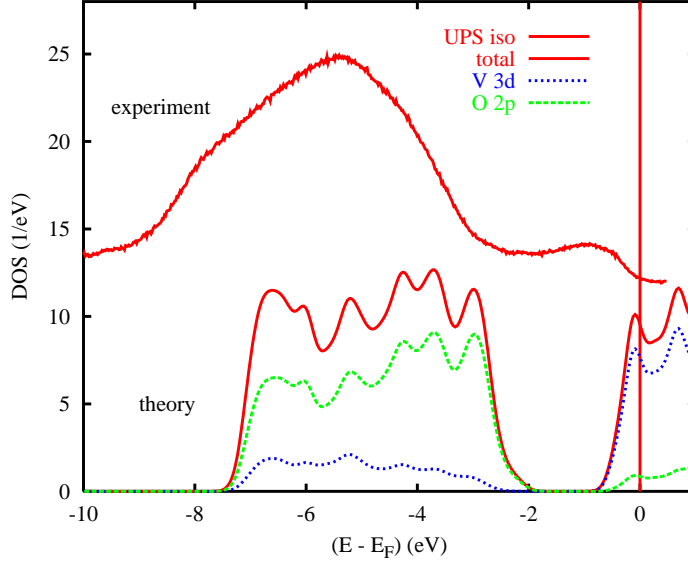


**Fig. 27** Total and partial densities of states (DOS) of monoclinic VO<sub>2</sub> folded with a 0.25 eV wide Gaussian (lower set of curves) and UPS spectra (upper curve; note the offset introduced in order to distinguish experimental and theoretical results; from Ref. [43, 45]).

densities of states. The curves are folded with a Gaussian of 0.25 and 0.5 eV width, respectively, for the occupied and unoccupied part of the spectrum. Good agreement with the XPS and UPS spectra by Blaauw *et al.*, Shin *et al.*, Bermudez *et al.*, and Goering *et al.* is found [46, 41, 42, 43, 45]. Data by the latter group were added in Fig. 27. According to these experiments the UPS spectra taken in the metallic and the insulating phase are very similar with respect to the oxygen dominated bands but show distinct differences in the low-binding region. They arise from a sharpening and slight downshift of the V  $3d$ -derived peak [46, 41, 43, 45]. As a comparison of Fig. 27 with Fig. 14 reveals, this experimental result is well accounted for by our calculations except for the fact that the V  $3d$  downshift is underestimated.

More striking differences between metallic and insulating VO<sub>2</sub> are observed in the soft-X-ray absorption spectra (XAS) as measured by Müller *et al.* [90, 48], which we

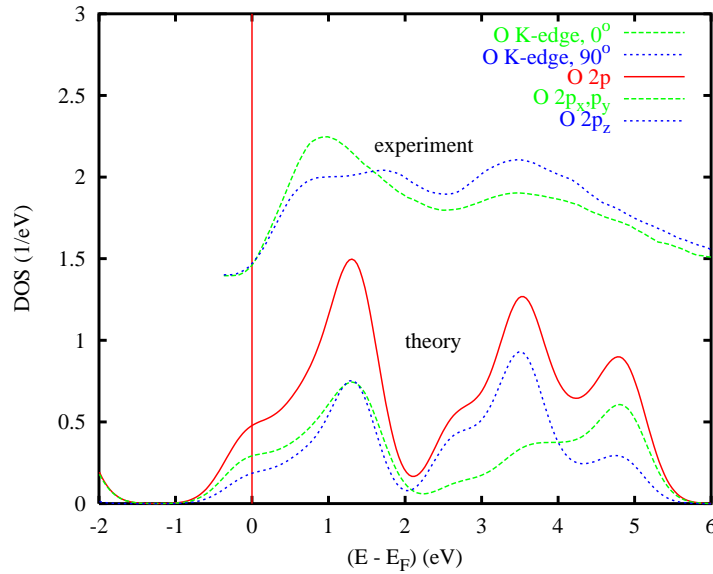


**Fig. 28** Partial O  $2p$  densities of states (DOS) of monoclinic  $\text{VO}_2$  folded with a 0.5 eV wide Gaussian (lower set of curves) and XAS O K edge spectra (upper set of curves; note the offset introduced in order to distinguish experimental and theoretical results; from Ref. [90, 48], data shifted by 529.5 eV).

display in Fig. 28. The experimental data were shifted by 529.5 eV. As already described in Sec. 5.4, the XAS spectra allowed to probe the angular dependence by varying the orientation of the polarization vector  $\mathbf{E}$  from parallel ( $\phi = 90^\circ$ ) to perpendicular ( $\phi = 0^\circ$ ) to the rutile  $c$  axis. Dipole selection rules then allow for transitions from O  $1s$  to either the O  $2p_z$  or the O  $2p_x$  and  $2p_y$  states. This is reflected by the calculated partial DOS of the corresponding final states. However, note that the curve marked O  $2p_x, p_y$  actually comprises only the mean average of these orbitals since the component perpendicular to  $\mathbf{E}$  is not seen in experiment. For the same reason, the curve marked O  $2p$  actually contains the full contribution from the  $p_z$  orbital but only half of the contributions from the  $p_x$  and  $p_y$  orbitals.

According to the experiments by Müller *et al.* as well as by Abbate *et al.* major differences between the XAS spectra of metallic and insulating  $\text{VO}_2$  originate from the appearance of an additional peak in the low-temperature phase [90, 48, 47]. In the spectra by Abbate *et al.* this new peak is located at 530.9 eV and seems to have split off from the peak at 529.9 eV, which, like the one at 532.5 eV, exists also in the metallic phase [47]. Abbate *et al.* interpreted the additional peak as arising from an upshift of the antibonding  $d_{||}$  band by about 1 eV. The other two  $t_{2g}$  bands, namely the  $\pi^*$  bands, stay at their original position. The XAS curves taken by Müller *et al.* are almost identical to the results of Abbate *et al.*. However, in a more detailed fit Müller assigned the spectra to five different peaks at 529.9, 530.4, 531.2, 532.7, and 533.9 eV [90].

Again, there is an overall good agreement between experiment and theory with

respect to positions, intensities, and angular dependencies of the peaks. As a comparison with Fig. 15 reveals, the calculated curves reflect the upshift of the O  $2p_z$  peak from 0.7 eV to 1.3 eV, which is the position of the upper  $d_{x^2-y^2}$  peak in Fig. 24. At the same time, all other peaks hardly move. Nevertheless, the O  $2p_z$  peak has its maximum at the same energy as the O  $2p_x, p_y$  curve at 1.3 eV. This is in contrast to the XAS experiments, which find the maximum of the O  $2p_z$  peak near 1.8 eV. Thus, it seems that the upshift of the O  $2p_z$  states and, hence, of the upper  $d_{x^2-y^2}$  states, is underestimated by the calculation in the same manner as in our previous work on MoO<sub>2</sub> [23]. From a comparison of the calculated DOS with both angle-resolved UPS and XAS data for the molybdenum dioxide, we obtained perfect agreement with experiment except for the bonding and antibonding Mo  $4d_{x^2-y^2}$  bands. Their splitting was underestimated by about 1 eV. For VO<sub>2</sub> the calculations yield a separation of  $\approx 1.7$  eV between the bonding and antibonding  $d_{x^2-y^2}$  bands. A value of 2.0 to 2.5 eV has been extracted from UPS and XAS measurements [41, 47].

Finally, as for rutile VO<sub>2</sub> the calculated high-energy peak at  $\approx 4.8$  eV gives rise to only a very slight shoulder in the experimental curve. Yet, it can be fully resolved by the aforementioned five peak analysis by Müller [90].

#### 6.4 Embedded Peierls instability

The upshift of the V  $3d_{xz}$  and  $d_{yz}$  bands as well as the bonding-antibonding splitting of the  $d_{x^2-y^2}$  band as observed in the partial DOS already signaled the general validity of the mechanism proposed by Goodenough and, more recently, by Wentzcovitch *et al.* [6, 7, 8]. Nevertheless, we still aim at obtaining more direct support for these ideas from the electronic structure. In order to prepare for the discussion we display in Fig. 29 the weighted band structure of rutile VO<sub>2</sub> corresponding to the  $d_{x^2-y^2}$  states. It results from that shown in Fig. 19 by backfolding to the monoclinic Brillouin zone, Fig. 10(b). As before the length of a bar given with a band at a  $\mathbf{k}$ -point is a measure of the contribution from the  $d_{x^2-y^2}$  orbital. Note that again we refer to the local reference frame.

In Fig. 29 we observe an arrangement of the  $d_{x^2-y^2}$  bands in two parts below and above 0.4 eV, respectively. They are connected by dispersing bands especially along the lines  $\Gamma$ -A and  $\Gamma$ -B. Both lines have components perpendicular to the rutile basal plane and correspond to half the line  $\Gamma$ -R of the tetragonal Brillouin zone. In contrast, the dispersion parallel to the rutile basal plane is suppressed to a large degree. The respective bands stay at energies either well below or above 0.4 eV, even if there is some dispersion within the lower group. Finally,  $d_{x^2-y^2}$  bands along the lines A-E and B-D, while likewise displaying a reduced dispersion, stay at an intermediate energy in the middle between the two subgroups. Note that these lines lie completely within horizontal planes at height  $\frac{\pi}{2c}$ . The general characteristics of these bands are thus very similar to those of the  $4d_{x^2-y^2}$  bands of hypothetical rutile MoO<sub>2</sub>. In that system the dispersionless bands along A-E and B-D were responsible for the flat portions of the Fermi surface. They were thus interpreted as driving the Peierls-type instability of this structure.

The V  $3d_{xz}$  and  $d_{yz}$  bands can be identified in Fig. 29 as the states without a bar. This interpretation is based on the fact that the O  $2p$  and the V  $3d e_g$  states play

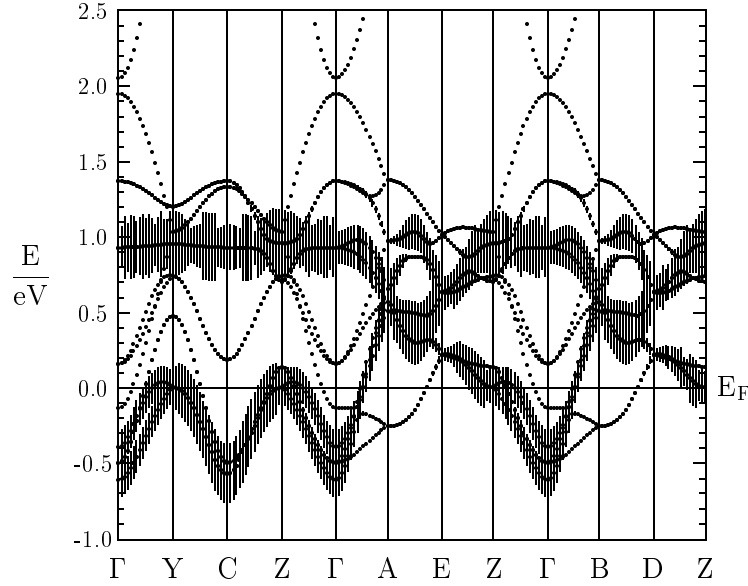


**Fig. 29** Weighted electronic bands of rutile  $\text{VO}_2$ . The width of the bars given for each band indicates the contribution due to the  $3d_{x^2-y^2}$  orbital of the V atom at the corner of the rutile cell relative to the local rotated reference frame.

only a minor role in the energy range shown. In contrast to the  $d_{x^2-y^2}$  bands these  $\pi^*$  bands do not fall into energetically lower and upper bands. Instead they rather show isotropic dispersion. Finally, we note again the much reduced hybridization between both types of bands, which we already mentioned at the end of Sec. 5.6. As a consequence, the  $d_{\parallel}$  and  $\pi^*$  bands can, as before, be regarded as nearly independent.

The corresponding weighted band structure for monoclinic  $\text{VO}_2$  is shown in Fig. 30. The differences between both figures is striking. On going from rutile to monoclinic  $\text{VO}_2$  we observe a strong splitting of the  $d_{x^2-y^2}$  bands into two narrow subbands at the lower and upper edge of the  $t_{2g}$  group of bands. This splitting is a consequence of the metal-metal dimerization. In the partial DOS, Fig. 24, this bonding-antibonding splitting led to the formation of the two distinct peaks just below  $E_F$  and at  $\approx 1.3$  eV. In particular, the  $d_{x^2-y^2}$  bands along the lines  $\Gamma$ -A-E-Z and  $\Gamma$ -B-D-Z have moved downward and upward, respectively, by about 0.5 eV relative to their positions in the rutile structure. As a consequence, the so far unoccupied branch of these bands between  $E_F$  and  $\approx 0.4$  eV has become almost fully occupied and the Fermi surface due to the  $d_{x^2-y^2}$  states has almost vanished. Moreover, these changes explain the occurrence of the split-off double band at the lower edge of the  $t_{2g}$  group of bands, which we mentioned at the end of Sec. 6.1.

In contrast, the V  $3d_{xz}$  and  $d_{yz}$  bands, i.e. those bands in Fig. 30, which have bars of negligible lengths, experience a considerable upshift by  $\approx 0.5$  eV due to the zigzag-like antiferroelectric displacement of the vanadium atoms. This result is in full agreement with the data by Shin *et al.* [41]. Yet, with only minor exceptions, the shift

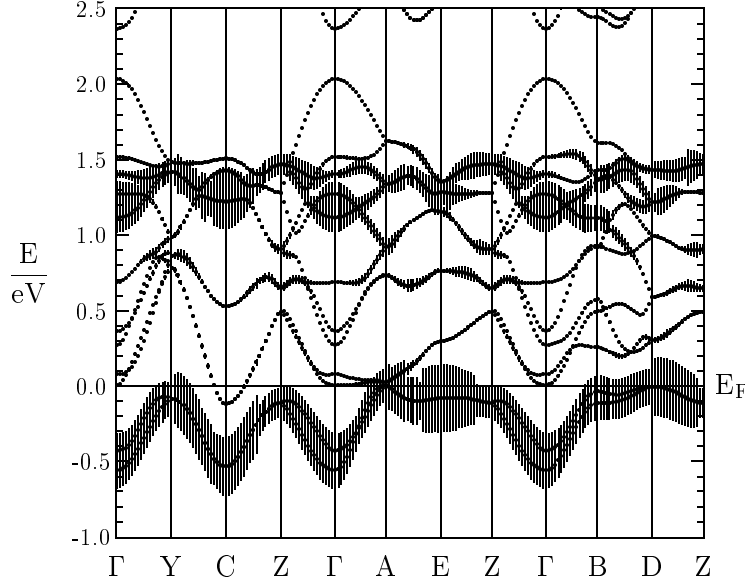


**Fig. 30** Weighted electronic bands of monoclinic VO<sub>2</sub>. The width of the bars given for each band indicates the contribution due to the  $3d_{x^2-y^2}$  orbital of the V atom at the corner of the rutile cell relative to the local rotated reference frame.

of the  $\pi^*$  bands leaves the general topology of these bands intact and causes their almost complete depopulation. Our findings agree well with the arguments given by Goodenough, who concluded from the isotropic conductivity that the  $\pi^*$  states should be located at the lower edge of the conduction band well below the antibonding  $d_{||}$  band [7]. Furthermore, Goodenough deduced from the measured low Hall mobility a narrowing of the  $\pi^*$  bands [7]. Indeed, our calculations result in a band width of about 2 eV of the  $\pi^*$  bands, which is considerably less than the 2.5 eV found in the rutile phase.

Finally, we note that the hybridization between both types of bands is still very small. In other words, the just described changes of the  $d_{||}$  and  $\pi^*$  bands occurred rather independently. The coupling between them is still only via the common Fermi energy. Just in the same manner as in NbO<sub>2</sub> and MoO<sub>2</sub> we may thus regard the transition to the low-temperature state as a Peierls instability of the  $d_{||}$  bands in an embedding background of  $\pi^*$  electrons.

An aspect, which seemingly has not been considered before, arises from the fact, that metal-metal pairing along the rutile  $c$  axis, in addition to increasing the bonding-antibonding splitting of the  $d_{x^2-y^2}$  bands, shifts the vanadium atoms also *relative* to the surrounding oxygen octahedra and, hence, causes an increased metal-oxygen overlap. Thus, if not compensated by a corresponding displacement of the oxygen octahedron, the dimerization likewise brings in an antiferroelectric component. As a consequence, within an investigation of the monoclinic M<sub>1</sub> structure we are actually not able to uniquely attribute the upshift of the  $\pi^*$  bands to either the zigzag-type in-

plane displacement or the metal-metal pairing. This is due to the fact that in the  $M_1$  phase all metal chains experience the same atomic displacements. The issue can only be resolved by studying the monoclinic  $M_2$  phase, which brings in a disproportionation of the vanadium chains.

## 7 Results for insulating $M_2$ -VO<sub>2</sub>

In the previous two sections we have investigated in detail both the metallic rutile and the insulating monoclinic ( $M_1$ ) phase of VO<sub>2</sub>. In addition, we proposed a possible explanation for the origin of the metal-insulator transition in terms of an embedded Peierls-like instability. Our conclusions confirmed the previous findings of Wentzcovitch *et al.*, who, using a molecular dynamics type approach, arrived at very similar results [8, 9]. Still, the discussion by these authors was criticized by Rice *et al.*, who focused attention on the monoclinic  $M_2$  phase of VO<sub>2</sub> [13].

The arguments given by Rice *et al.* aimed at attempts to explain the metal-insulator transition of stoichiometric VO<sub>2</sub> purely in terms of the dimerization in the monoclinic  $M_1$  phase. If this were the only or the dominating driving force there would be no reason why VO<sub>2</sub> in the  $M_2$  phase would be insulating, since only half of the chains dimerize. Yet, as has been already pointed out by Goodenough, metal-metal pairing is not the only source of an efficient splitting of the  $d_{||}$  band but the same effect could be achieved by exchange splitting coming with the antiferromagnetic order [6, 7]. The latter was indeed observed on the zigzag chains of the  $M_2$  structure. Nevertheless, from the antiferromagnetic ordering several authors concluded that the respective  $3d$  electrons would be rather localized and, while being accessible to strong electron-electron correlations, resist a proper description within band theory. Due to the close relation between the low-temperature monoclinic phases these arguments would then also hold for the  $M_1$  phase.

Since the  $M_2$  phase has not yet been considered using state-of-the-art electronic structure calculations we included its investigation in the present study. From discussion of the  $M_2$  phase we expect a deeper understanding of the mechanisms, which are active in the  $M_1$  phase, since each chain shows only one type of octahedral deformation. Furthermore, we should be able to distinguish the different types of vanadium atom displacements with respect to their coupling to the electronic states and, in particular, to identify the implications of the two different types of antiferroelectric modes arising from the zigzag-type and pairing displacements. The latter can not be resolved in investigations of the  $M_1$  phase.

As has been outlined in Sec. 2.3, Pouget *et al.* proposed to view the monoclinic  $M_2$  phase as a metastable modification of the  $M_1$  phase and to regard both the doping with Cr or Al and the application of uniaxial stress as only small perturbations of pure VO<sub>2</sub> under ambient pressure. These arguments were supported by the crystal structure data reported for different types of dopants. For both the rutile and the  $M_2$  phase the parameters given by Marezio *et al.* for V<sub>0.976</sub>Cr<sub>0.024</sub>O<sub>2</sub> and by Ghedira *et al.* for V<sub>0.985</sub>Al<sub>0.015</sub>O<sub>2</sub> are almost identical [20, 66] and for the rutile structure they are identical to the numbers given for stoichiometric VO<sub>2</sub>, see Sec. 3.1 and Tabs. 5 and 6. It is thus well justified to use the crystal structure data for the doped material

as input for the present study of the M<sub>2</sub> phase.

Our investigations for the M<sub>2</sub> phase proceeded in two steps. First we performed calculations using the crystal structure data given by Marezio *at al.* and assuming spin-degeneracy. Spin-polarization was included in a second step. This way we were able to check the stability of the antiferromagnetic state with respect to the spin-degenerate case. Furthermore, our procedure allowed to separate the impact of the structural transformations and magnetic order on the electronic structure.

### 7.1 Non-spinpolarized calculations

We display in Fig. 31 the electronic states along selected high symmetry lines within

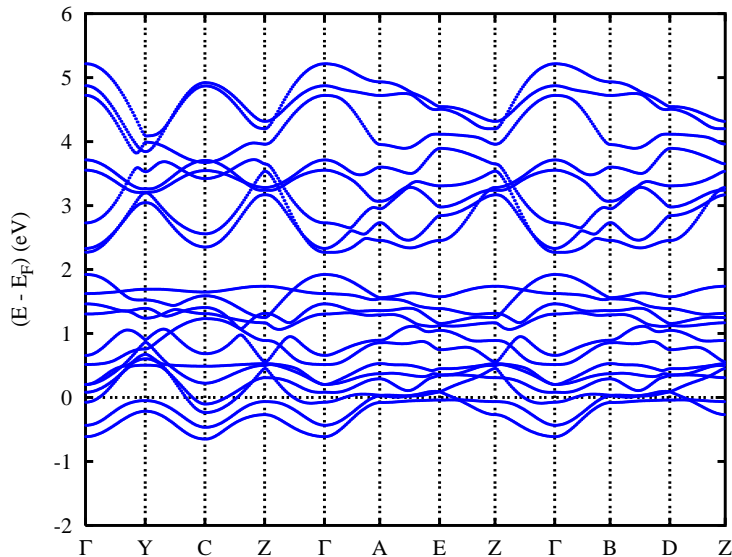


**Fig. 31** Electronic bands of monoclinic M<sub>2</sub> VO<sub>2</sub> along selected symmetry lines within the simple monoclinic Brillouin zone.

the centered monoclinic Brillouin zone. Except for the small lattice strain, which distorts the basal plane, the latter Brillouin zone is identical to the simple monoclinic Brillouin zone of the M<sub>1</sub> phase. The dominant partial densities of states (DOS) are given in Fig. 32. As for the M<sub>1</sub> phase of VO<sub>2</sub> we observe many similarities with the rutile results as concerns the ordering, widths and separations of the bands. Still, we find the O 2*p*-, V 3*d t*<sub>2*g*</sub>- and *e*<sub>*g*</sub>-dominated groups of bands below, at and above the Fermi energy, respectively, as well as a hybridization of these states of the order of 10%.

Differences between the results for the two low-temperature phases show up on closer inspection of the V 3*d* derived partial DOS. Due to the presence of two different chains in the M<sub>2</sub> phase we have distinguished the two types of vanadium atoms, namely V<sub>1</sub> and V<sub>2</sub>, which belong to the dimerizing and the zigzag chains, respectively. Distinct differences occur in the *t*<sub>2*g*</sub> group of bands. The V<sub>1</sub> 3*d t*<sub>2*g*</sub> partial DOS displays strong

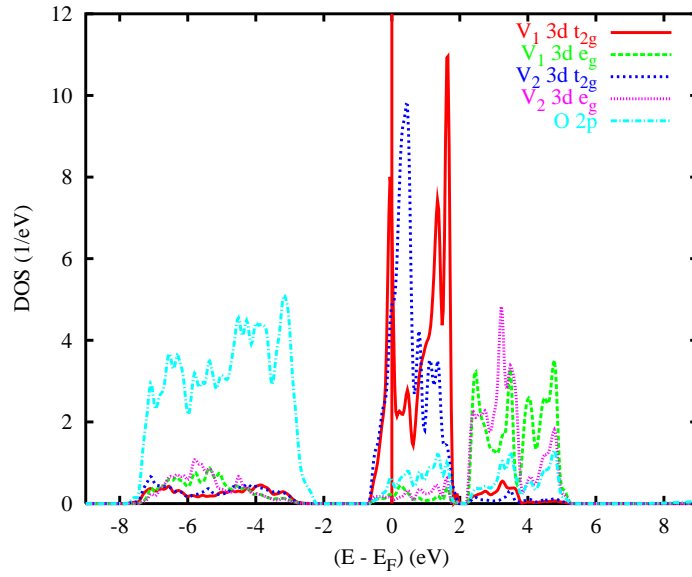


**Fig. 32** Partial densities of states (DOS) of monoclinic  $M_2$   $VO_2$  per unit cell.

splitting into two peaks just below  $E_F$  and at  $\approx 1.8$  eV similar to that observed for the  $M_1$  phase, Fig. 23. In contrast, the  $V_2$   $3d t_{2g}$  partial DOS is dominated by a single maximum at  $\approx 0.3$  eV and resembles the respective partial DOS found for the rutile structure, Fig. 11. Qualitatively, the same holds for the  $V$   $3d e_g$  partial DOS, for which we note the close similarity of the partial DOS assigned to the  $V_1$  and  $V_2$  atoms to those calculated for the  $M_1$  and the rutile structure. All these findings reflect our expectations. In a non-spinpolarized calculation the dimerizing and zigzag chains should display similar behaviour as that known from the  $M_1$  and the rutile phase, respectively.

Going into more detail we display in Figs. 33 and 34 the  $3d$  partial DOS of the  $V_1$  and  $V_2$  atoms as decomposed into their symmetry components relative to the respective local reference frame of each chain. As for the rutile and the  $M_1$  phase we observe for both types of vanadium atoms the energetical separation of the  $3d t_{2g}$  and  $e_g$  groups of bands resulting from the crystal field splitting. However, within these groups of bands we also witness the aforementioned differences between the  $V_1$  and  $V_2$  atoms.

The  $t_{2g}$  partial DOS of the paired  $V_1$  atoms closely resemble the  $t_{2g}$  partial DOS of the  $M_1$  phase as given by Fig. 24. They both are characterized by the strong bonding-antibonding splitting of the  $d_{x^2-y^2}$  states, which is even more pronounced in the  $M_2$  phase. This result fully agrees with the NMR data, which revealed the strong similarity of the Knight shift due to the dimerized vanadium atoms to that measured in the  $M_1$  phase [64]. In contrast, the  $d_{x^2-y^2}$  partial DOS of the  $V_2$  atoms, which belong to the zigzag chains, display a completely different behaviour. These states do not show any splitting but form a single maximum at  $\approx 0.4$  eV with a broad shoulder extending to  $-0.65$  eV and only minor contributions at energies above  $\approx 0.7$ . This

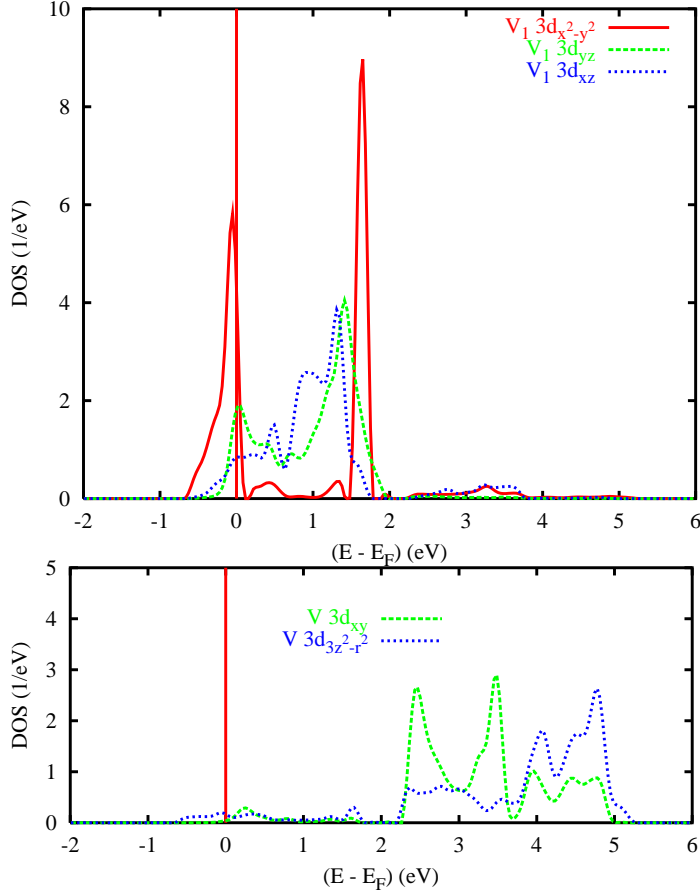


**Fig. 33** Partial V<sub>1</sub> 3d  $t_{2g}$  and  $e_g$  densities of states (DOS) of monoclinic M<sub>2</sub> VO<sub>2</sub>. Selection of orbitals is relative to the local rotated reference frame.

shape thus bears a strong similarity to the corresponding DOS of the rutile phase, see Fig. 12, rather than to that of the monoclinic M<sub>1</sub> phase. To conclude, the  $d_{x^2-y^2}$  partial DOS can be readily understood from the local environment of the respective atoms as being more M<sub>1</sub>- and rutile-like, respectively.

The  $d_{xz}$  and  $d_{yz}$  curves follow this general trend in that the V<sub>1</sub> partial DOS reflect the behaviour known from the M<sub>1</sub> phase while the V<sub>2</sub> partial DOS are more rutile-like. Yet, two features are worth mentioning: i) The splitting of the  $3d_{yz}$  partial DOS as observed in the rutile structure is almost completely suppressed on the V<sub>2</sub> chains. This is due to the zigzag-like displacement of these atoms, which undermines the in-plane overlap of the  $d_{yz}$  orbitals and, hence, reduces their bonding-antibonding splitting. ii) The upshift of the  $\pi^*$  states affects *both* the V<sub>1</sub> and the V<sub>2</sub> partial DOS. From the discussion in Sec. 6, where we attributed the upshift of these bands to the antiferroelectric mode of the vanadium atoms coming with the zigzag-like in-plane displacements, we would have expected a raise in energy *only* for the  $\pi^*$  states of the

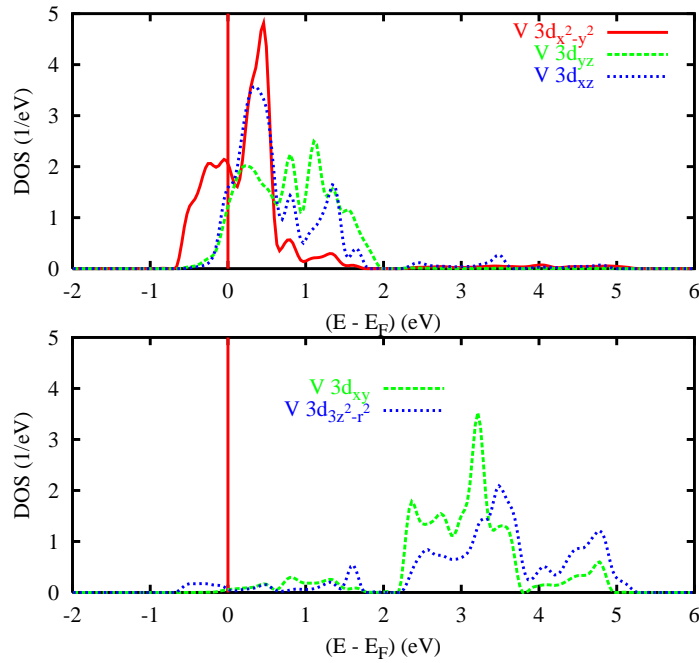


**Fig. 34** Partial  $V_2$   $3d$   $t_{2g}$  and  $e_g$  densities of states (DOS) of monoclinic  $M_2$   $VO_2$ . Selection of orbitals is relative to the local rotated reference frame.

$V_2$  atoms but not for the vanadium atoms in the dimerizing chains. Yet, a closer look at the partial DOS in Figs. 33 and 34 reveals that the centers of gravity of the  $\pi^*$  bands actually is higher on the dimerizing chains.

An explanation for this latter behaviour can be found in an analysis of the possible metal-oxygen overlaps using Tab. 13, where we combine those particular  $V$   $3d$   $t_{2g}$  and

**Table 13**  $V$   $3d$ - $O$   $2p$  orbital overlaps.

	$O_1$	$O_2$	$O_3$
$V_1$ $3d_{x^2-y^2}$		$2p_x, 2p_y$	$2p_x, 2p_y$
$V_1$ $3d_{xz}$	$2p_x$	$2p_z$	$2p_z$
$V_1$ $3d_{yz}$	$2p_y$	$2p_z$	$2p_z$
$V_2$ $3d_{x^2-y^2}$	$2p_x, 2p_y$		
$V_2$ $3d_{xz}$		$2p_x$	$2p_x$
$V_2$ $3d_{yz}$		$2p_y$	$2p_y$

$O$   $2p$  orbitals, which, within a molecular-orbital picture, are expected to overlap. We complement the table with the partial  $O$   $2p$  partial DOS in Fig. 35, where we have

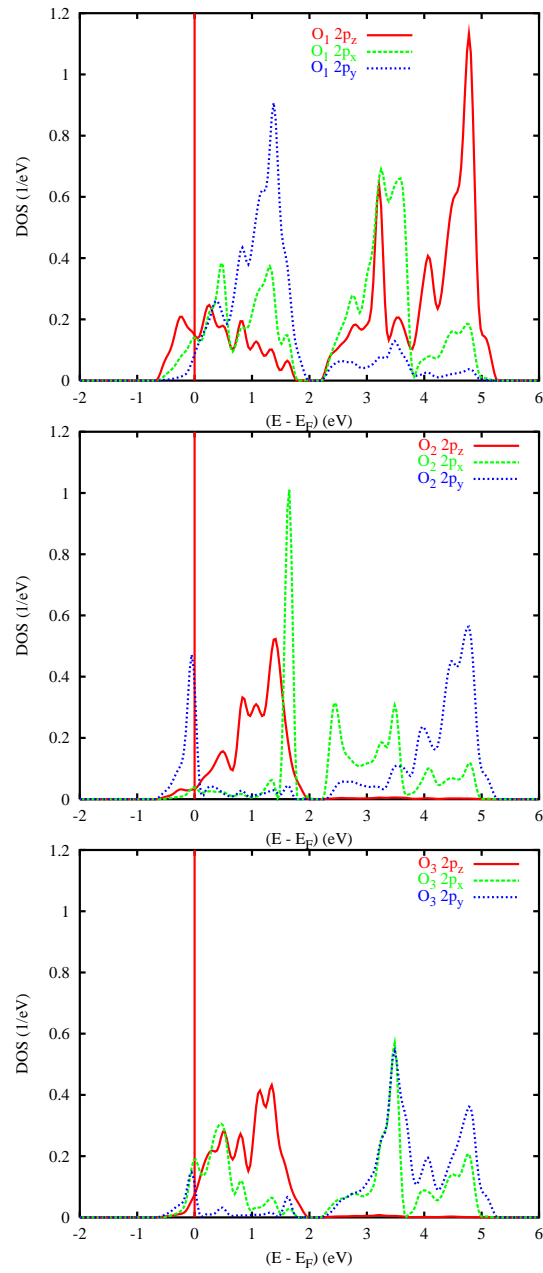


**Fig. 35** Partial O 2p densities of states (DOS) of monoclinic M<sub>2</sub> VO<sub>2</sub>. Selection of orbitals is relative to the local rotated reference frame of atom V<sub>1</sub>.

again used the local rotated frame of reference for the selection of the orbitals. Note that we opted for the local reference frame corresponding to the dimerizing  $V_1$  chains. As outlined in Sec. 3.1 interpretation in terms of the reference frame of the zigzag-like  $V_2$  chains simply requires exchange of the  $y$  and  $z$  components. For the following discussion we recall that the  $O_1$  atoms are the apical oxygen atoms of the dimerizing  $V_1$  chains and occupy the equatorial positions of the zigzag-like  $V_2$  chains, see Fig. 7. For oxygen atoms  $O_2$  and  $O_3$  things are reversed with the latter having the shorter distance to the central  $V_2$  atom. In addition, due to the dimerization,  $O_2$  have a very short bond with the vanadium atoms of type  $V_1$ .

The aforementioned geometry is reflected by the partial DOS. In Fig. 35 we observe a striking similarity of the partial DOS corresponding to atom  $O_2$  to the  $V_1$   $3d$  partial DOS as shown in Fig. 33. In general, all contributions in Figs. 33 to 35 can be well understood using the orbital overlaps listed in Tab. 13. In particular, we observe the hybridization of the  $V_2$   $3d_{xz}$  peak at  $\approx 0.4$  eV with the  $O_3$   $2p_x$  contribution. Onset of the zigzag-like mode increases this overlap and shifts these states to higher energies. In contrast, the  $V_1$   $3d_{xz}$  states, which are found mainly above 0.8 eV, overlap with the  $2p_z$  states of their equatorial  $O_2$  and  $O_3$  partners. This overlap increases with increasing dimerization on these chains and, hence, also causes an upshift in energy. We thus witness a considerable antiferroelectric component of the metal-metal pairing, which drives upshift of the  $\pi^*$  states on the corresponding chains and which we already proposed at the end of Sec. 6.4.

The interpretation of the results found especially for the  $d_{x^2-y^2}$  partial DOS of the two different types of chains is confirmed by the weighted band structures as displayed in Figs. 36 and 37. Again we note the energetical upshift of the  $d_{xz}$  and  $d_{yz}$  bands, which is almost independent of the type of chain, on which these orbitals are located. The  $d_{x^2-y^2}$  bands of the  $V_1$  atoms show the strong bonding-antibonding splitting already observed in the partial DOS, Fig. 33, in complete analogy to the weighted  $d_{x^2-y^2}$  bands of the  $M_1$  phase, Fig. 30. In both phases it results from the metal-metal pairing on the respective chains and leads to the semimetallic behaviour of these bands with a clear separation of bands of different characters. The same effect was already observed in the results for the  $M_1$  structure. In contrast, the  $d_{x^2-y^2}$  bands of the  $V_2$  atoms, which have equal metal-metal distances, resemble the dispersion of these bands in the rutile structure, see Fig. 29. Their reduced band width, which is by  $\approx 0.4$  eV smaller as compared to the rutile structure, reflects the increased  $V_2$ - $V_2$  distance in the zigzag chains. Nevertheless, these bands still display the one-dimensional dispersion found for the rutile phase. As a consequence, from the spin-degenerate calculations we obtain half-filled  $V_2$   $d_{x^2-y^2}$  bands of  $\approx 1.1$  eV width, which are clearly metallic. To conclude, enforcing spin-degeneracy we find indications for a metal-insulator transition very similar to those discussed in Sec. 6 in the dimerizing chains but at the same time we obtain rutile-like metallic behaviour due to the bands originating from states on the zigzag chains.

## 7.2 Spinpolarized calculations

Next we turn to the spinpolarized calculations as suggested by the experimental finding of antiferromagnetic Heisenberg chains in the  $M_2$  phase of  $VO_2$ . As a result we obtain

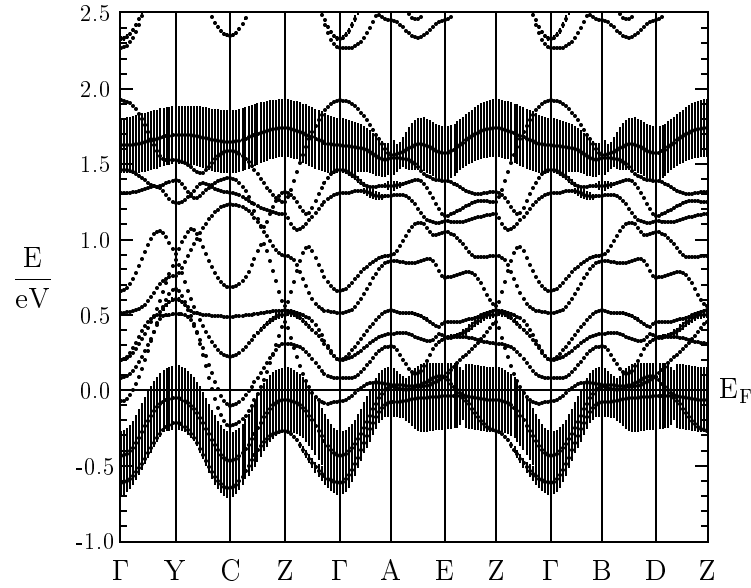


**Fig. 36** Weighted electronic bands of monoclinic M<sub>2</sub> VO<sub>2</sub>. The width of the bars given for each band indicates the contribution due to the  $3d_{x^2-y^2}$  orbital of atom V<sub>1</sub>, which belongs to a dimerizing chain, relative to the local rotated reference frame.

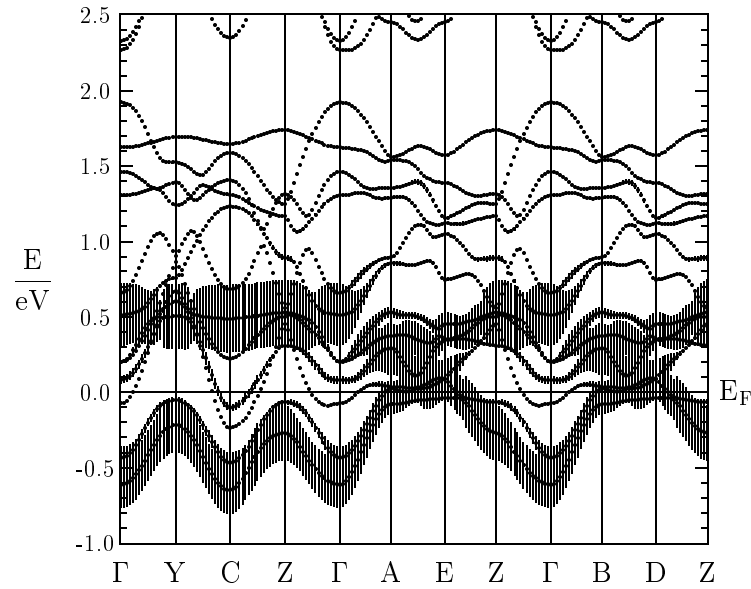


**Fig. 37** Weighted electronic bands of monoclinic M<sub>2</sub> VO<sub>2</sub>. The width of the bars given for each band indicates the contribution due to the  $3d_{x^2-y^2}$  orbital of atom V<sub>2</sub>, which belongs to a zigzag chain, relative to the local rotated reference frame.

a stable antiferromagnetic solution with a total energy, which is by 0.7 mRyd per unit cell lower than that growing out of the non-spinpolarized calculation. Magnetic moments of  $0.46 \mu_B$  are carried by the  $V_2$  3d states of the zigzag chains. The moments of all other atoms are either negligibly small or, for symmetry reasons, exactly zero as in case of the  $V_1$ . The dominant partial DOS are displayed in Fig. 38. Note

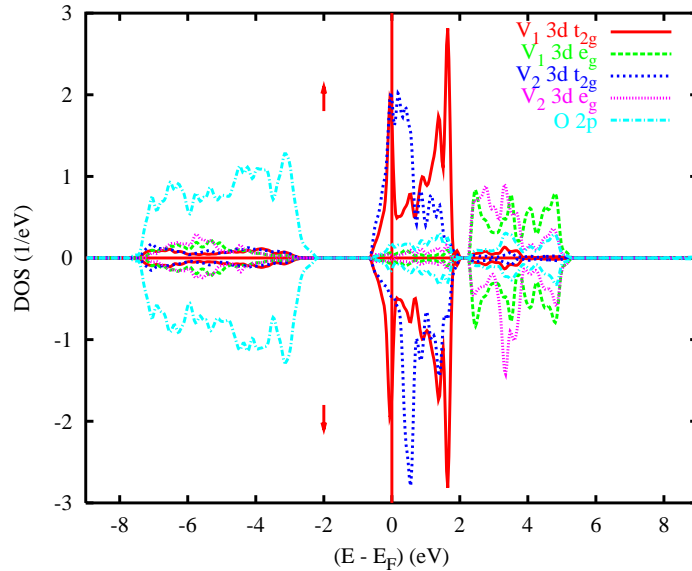


**Fig. 38** Partial densities of states (DOS) of antiferromagnetic monoclinic  $M_2$   $VO_2$  per unit cell.

that *all* curves in Fig. 38 comprise contributions from one magnetic sublattice only. On comparing Fig. 38 to Fig. 32 for the non-spinpolarized case we recognize the main changes arising from spinpolarization in the small energy interval from -1 to 1 eV about the Fermi energy. The  $V_1$  3d  $t_{2g}$  partial DOS are identical for both spin directions due to the vanishing magnetic moments at these sites. Spin splitting arises mainly from the  $V_2$  3d  $t_{2g}$  states. Their spin up and down DOS are dominated by a broader peak just above  $E_F$  and rather sharp peak at  $\approx 0.7$  eV, respectively.

The changes originating from antiferromagnetic order are reflected by analysis of the V 3d partial DOS, which we display in Figs. 39 and 40. Again, the identical spin up and down DOS of the  $V_1$  atoms reflect the vanishing magnetic moments of these atoms. In contrast, we observe spin-dependent shifts of the  $V_2$  partial DOS in the energy interval between -1 and 1 eV and, to a lesser degree, between 2 and 4 eV. While spin-splitting of the  $d_{xz}$  and  $d_{yz}$  states is rather small on these atoms the magnetic moment originates mainly from the local  $d_{x^2-y^2}$  states.

Recalling the non-spinpolarized  $d_{x^2-y^2}$  partial DOS as shown in Fig. 34 with its prominent peak at  $\approx 0.5$  eV and the broad shoulder below  $E_F$  we can now attribute the peak at 0.5 eV mainly to the spin down states while the broad shoulder comprises almost exclusively the spin up states. This situation becomes clearer from the weighted electronic structures as shown in Figs. 41 and 42. These band structures highlight

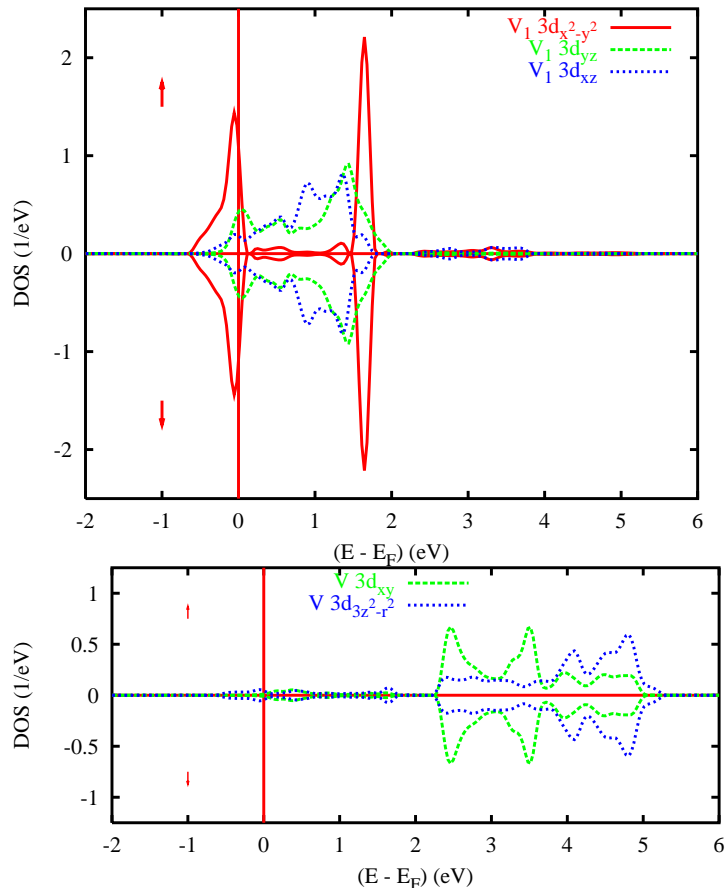


**Fig. 39** Partial  $V_1$   $3d$   $t_{2g}$  and  $e_g$  densities of states (DOS) of antiferromagnetic monoclinic  $M_2$  VO<sub>2</sub>. Selection of orbitals is relative to the local rotated reference frame.

the spin up and down  $V_2$   $3d_{x^2-y^2}$  bands relative to the local reference frame of the single atom belonging to the spin up sublattice. While the occupied  $3d_{x^2-y^2}$  bands are mainly of spin up character, bands at higher energies are almost exclusively of spin down character. The spin majority and minority bands thus play a similar role as the bonding and antibonding bands of the vanadium  $3d_{x^2-y^2}$  states located at the dimerizing chains. The spin majority states are almost completely filled and show only small contributions to the bands at  $\approx 0.6$  eV. In contrast, the spin minority states dominate the bands in the energy range between 0.4 and 0.6 eV. As a consequence, antiferromagnetic ordering is obtained in the zigzag chains. At the same time, singlet formation arises in the dimerizing chains.

As for the  $M_1$  phase, the band structures and densities of states calculated with the  $M_2$  structure lack the observed optical band gap. Yet, the situation is very similar to that found in Sec. 6. We find an overlap of the valence and conduction bands of  $\approx 0.2$  eV, which we attribute again to the shortcomings of the LDA. However, bands

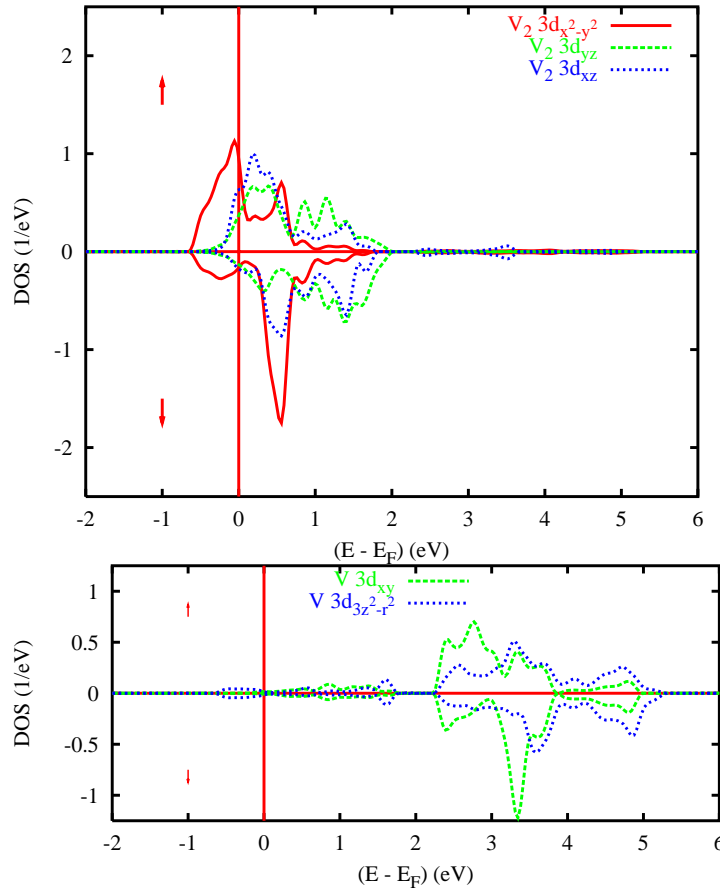


**Fig. 40** Partial  $V_2$   $3d$   $t_{2g}$  and  $e_g$  densities of states (DOS) of antiferromagnetic monoclinic  $M_2$   $VO_2$ . Selection of orbitals is relative to the local rotated reference frame.

of different orbital character are clearly separated. For this reason, it is well justified to regard DFT-based calculations as being capable to describe also the metal-insulator rutile-to- $M_2$  transition. This holds even if the opening of the optical band gap is just missed due to the LDA.

In summary, while the rutile phase is characterized by two types of rather weakly hybridized quasi-one-dimensional  $d_{\parallel}$  and isotropically dispersing  $\pi^*$  bands the changes in crystal structure and magnetic order coming with the  $M_2$  structure lead to distinct changes in the electronic structure. Both the zigzag-type displacement on the  $V_2$  chains and the dimerization on the  $V_1$  chains induce antiferroelectric shifts of the vanadium atoms inside the surrounding oxygen octahedra. The resulting increase of metal-oxygen bonding shifts the  $\pi^*$  bands to higher energies. In addition, dimerization of the  $V_1$  atoms causes splitting of the corresponding  $d_{\parallel}$  bands into bonding and antibonding branches. In contrast, the  $d_{\parallel}$  bands belonging to the  $V_2$  chains display spin-splitting and antiferromagnetic order in these chains. As for the  $M_1$  phase

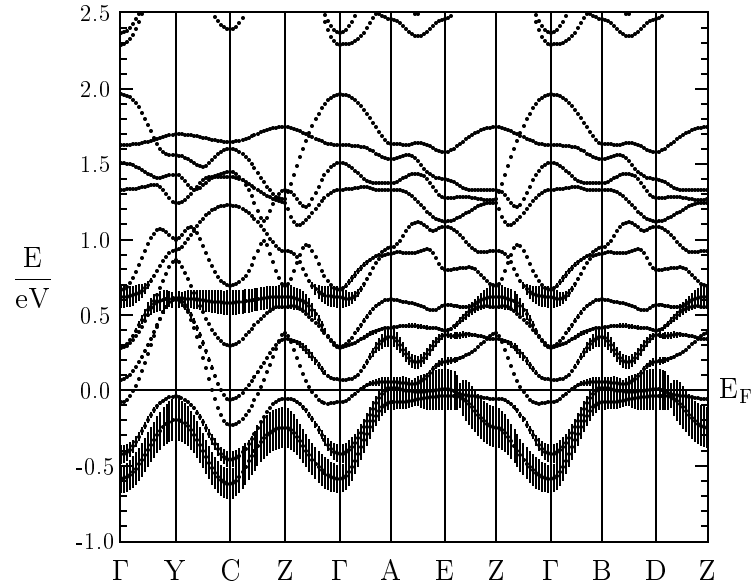


**Fig. 41** Weighted electronic bands of antiferromagnetic monoclinic M<sub>2</sub> VO<sub>2</sub>. The width of the bars given for each band indicates the contribution due to the spin up  $3d_{x^2-y^2}$  state of atom V<sub>2</sub>, which belongs to a zigzag chain, relative to the local rotated reference frame.

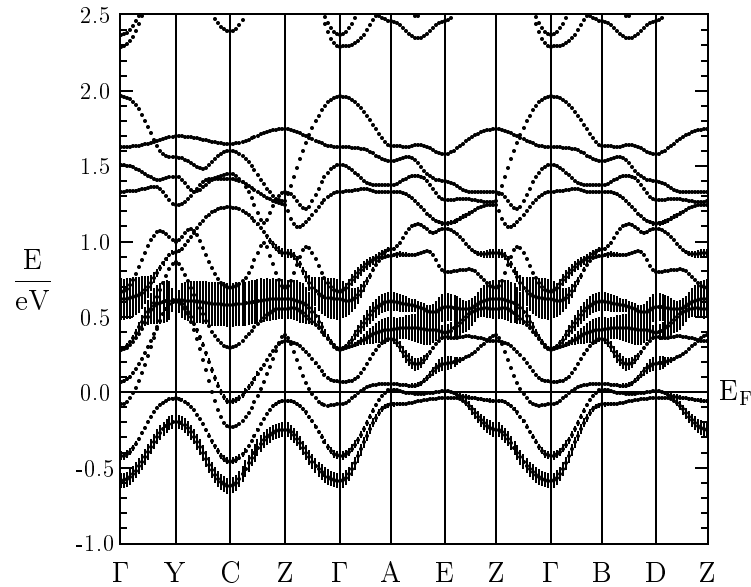


**Fig. 42** Weighted electronic bands of antiferromagnetic monoclinic M<sub>2</sub> VO<sub>2</sub>. The width of the bars given for each band indicates the contribution due to the spin down  $3d_{x^2-y^2}$  state of atom V<sub>2</sub>, which belongs to a zigzag chain, relative to the local rotated reference frame.

coupling between the different types of bands is still weak and mainly via the common Fermi energy. The scenario of an embedded Peierls instability proposed for the transition from the rutile to the  $M_1$  phase has to be extended by the possibility of antiferromagnetic ordering as already mentioned by Goodenough.

## 8 Conclusion

In the present first principles study, augmented spherical wave calculations were used to investigate the structural, electronic, and magnetic properties as well as the metal-insulator transitions of vanadium dioxide. The essential features of the metallic rutile as well as the insulating  $M_1$  and  $M_2$  phases are well described within DFT and LDA. In metallic  $VO_2$ , the electronic structure consists of oxygen  $2p$  bands well below the Fermi energy, as well as crystal field split vanadium  $3d$   $t_{2g}$  and  $e_g^\sigma$  bands. States near  $E_F$  consist of two very weakly hybridizing types of  $t_{2g}$  bands, namely, the  $d_{||}$  states with a quasi-one-dimensional dispersion parallel to the characteristic V chains, and isotropically dispersing  $e_g^\pi$  bands. In the low-temperature  $M_1$  structure of stoichiometric  $VO_2$ , metal-metal dimerization splits the  $d_{||}$  band into bonding and antibonding branches, whereas the  $e_g^\pi$  states shift to higher energies due to reduced V–O distances. Although, due to the imperfections of the LDA, semimetallic behaviour with a band overlap of  $\approx 0.1$  eV is obtained rather than the observed optical band gap, the  $d_{||}$  and  $e_g^\pi$  bands are completely separated. Since both types of bands are still coupled by charge conservation rather than hybridization, the insulating state is interpreted as due to a Peierls-like instability of the  $d_{||}$  bands in an embedding reservoir of  $e_g^\pi$  electrons. The situation is thus identical to the one previously found for  $MoO_2$  and  $NbO_2$  [23, 24], and gives rise to a unified picture for the transition-metal dioxides at the beginning of the  $d$  series. This approach explains both (i) the destabilization of the rutile structure in terms of increased metal-metal bonding and (ii) the metal-insulator transitions of the  $d^1$  members.

In the insulating  $M_2$  phase, obtained on doping or applying uniaxial pressure, which generally is viewed as a metastable phase of stoichiometric  $VO_2$ , the metal-insulator transition results from different, complementary mechanisms. Still, depopulation of the  $e_g^\pi$  states is due to the antiferroelectric components of both the zigzag-like displacements and the dimerization, which increase the metal-oxygen bonding. In addition, the embedded Peierls-like instability proposed for the rutile-to- $M_1$  transition causes bonding-antibonding splitting of the  $d_{||}$  bands connected with the dimerizing chains. In contrast, the  $d_{||}$  states located on the chains with equidistant vanadium atoms experience spin-splitting due to antiferromagnetic order of the localized moments, which are carried predominantly by the  $d_{||}$  electrons. As for the other phases, hybridization between the  $d_{||}$  and  $e_g^\pi$  states is very weak, and the transition can be interpreted as a combined embedded Peierls-like/antiferromagnetic instability of rutile  $VO_2$ .

I am grateful to U. Eckern, K.-H. Höck, S. Horn, and D. Vollhardt for their continuous support of this work as well as many helpful discussions. Thanks are also due to R. Horny, S. Klimm, D. Maurer, V. Müller, P. S. Riseborough, U. Schwingenschlögl, and W.-D. Yang for many fruitful discussions as well as to E. Goering and O. Müller for supplying the experimental data. This work was supported by the Deutsche Forschungsgemeinschaft (Forschergruppe

241 and Sonderforschungsbereich 484, Augsburg).

## References

- [1] F. J. Morin, Phys. Rev. Lett. **3** (1959) 34.
- [2] W. Brückner, H. Oppermann, W. Reichelt, J. I. Terukow, F. A. Tschudnowski, and E. Wolf, *Vanadiumoxide*, Akademie-Verlag, Berlin 1983.
- [3] J. B. Goodenough, Phys. Rev. **117** (1960) 1442.
- [4] D. Adler and H. Brooks, Phys. Rev. **155** (1967) 826.
- [5] D. Adler, J. Feinleib, H. Brooks, and W. Paul, Phys. Rev. **155** (1967) 851.
- [6] J. B. Goodenough, J. Solid State Chem. **3** (1971) 490.
- [7] J. B. Goodenough, *Metallic Oxides*, in: *Progress in Solid State Chemistry*, edited by H. Reiss, Pergamon Press, Oxford 1971, pp. 145-399.
- [8] R. M. Wentzcovitch, W. W. Schulz, and P. B. Allen, Phys. Rev. Lett. **72** (1994) 3389.
- [9] R. M. Wentzcovitch, W. W. Schulz, and P. B. Allen, Phys. Rev. Lett. **73** (1994) 3043.
- [10] N. F. Mott, Phil. Mag. **6** (1961) 287.
- [11] A. Zylbersztejn and N. F. Mott, Phys. Rev. B **11** (1975) 4383.
- [12] D. Paquet and P. Leroux-Hugon, Phys. Rev. B **22** (1980) 5284.
- [13] T. M. Rice, H. Launois, and J. P. Pouget, Phys. Rev. Lett. **73** (1994) 3042.
- [14] D. B. Rogers, R. D. Shannon, A. W. Sleight, and J. L. Gillson, Inorg. Chem. **8** (1969) 841.
- [15] L. F. Mattheiss, Phys. Rev. B **13** (1976) 2433.
- [16] V. Eyert, *Electronic structure calculations for crystalline materials*, in: *Density Functional Methods: Applications in Chemistry and Materials Science*, edited by M. Springborg, Wiley, Chichester 1997, pp. 233-304.
- [17] A. A. Bolzan, C. Fong, B. J. Kennedy, and C. J. Howard, Acta Cryst. B **53** (1997) 373.
- [18] G. Andersson, Acta Chim. Scand. **10** (1956) 623.
- [19] J. M. Longo and P. Kierkegaard, Acta Chim. Scand. **24** (1970) 420.
- [20] M. Marezio, D. B. McWhan, J. P. Remeika, and P. D. Dernier, Phys. Rev. B **5** (1972) 2541.
- [21] R. Pynn, J. D. Axe, and R. Thomas, Phys. Rev. B **13** (1976) 2965.
- [22] V. Eyert, Habilitation thesis, Universität Augsburg, 1998.
- [23] V. Eyert, R. Horny, K.-H. Höck, and S. Horn, J. Phys.: Cond. Matt. **12** (2000) 4923.
- [24] V. Eyert, Europhys. Lett. **58** (2002) 851.
- [25] K. Held, G. Keller, V. Eyert, D. Vollhardt, and V. I. Anisimov, Phys. Rev. Lett. **86** (2001) 5345.
- [26] K. Held, I. A. Nekrasov, G. Keller, V. Eyert, N. Blümer, A. K. McMahan, R. T. Scalettar, T. Pruschke, V. I. Anisimov, and D. Vollhardt, *The LDA+DMFT Approach to Materials with Strong Electronic Correlations*, in: *Quantum Simulations of Complex Many-Body Systems: From Theory to Algorithms*, edited by J. Grotendorst, D. Marx, and A. Muramatsu, NIC Series Volume 10, Forschungszentrum Jülich, 2002, p. 175-209.
- [27] D. B. McWhan, M. Marezio, J. P. Remeika, and P. D. Dernier, Phys. Rev. B **10** (1974) 490.
- [28] J. Y. Prieur, P. Seznec, S. Ziolkiewicz, J. Phys. Lett. **38** (1977) L25.
- [29] K. V. K. Rao, S. V. N. Naidu, and L. Iyengar, J. Phys. Soc. Jap. **23** (1967) 1380.
- [30] D. Kucharczyk and T. Niklewski, J. Appl. Cryst. **12** (1979) 370.
- [31] J. P. Pouget and H. Launois, J. Phys. (France) **C4-37** (1976) 49.
- [32] S. Minomura and H. Nagasaki, J. Phys. Soc. Jap. **19** (1964) 131.
- [33] T. Kawakubo and T. Nakagawa, J. Phys. Soc. Jap. **19** (1964) 517.
- [34] D. Maurer, A. Leue, R. Heichele, and V. Müller, Phys. Rev. B **60** (1999) 13249.
- [35] H. Terauchi and J. B. Cohen, Phys. Rev. B **17** (1978) 2494.
- [36] J. R. Brews, Phys. Rev. B **1** (1970) 2557.
- [37] F. Gervais and W. Kress, Phys. Rev. B **31** (1985) 4809.
- [38] E. I. Terukov, W. Reichelt, M. Wolf, H. Hemschik, and H. Oppermann, phys. stat. sol. (a) **48** (1978) 377.

- [39] H. W. Verleur, A. S. Barker, Jr., and C. N. Berglund, *Phys. Rev.* **172** (1968) 788.
- [40] R. J. Powell, C. N. Berglund, and W. E. Spicer, *Phys. Rev.* **178** (1969) 1410.
- [41] S. Shin, S. Suga, M. Taniguchi, M. Fujisawa, H. Kanzaki, A. Fujimori, H. Daimon, Y. Ueda, K. Kosuge, and S. Kachi, *Phys. Rev. B* **41** (1990) 4993.
- [42] V. M. Bermudez, R. T. Williams, J. P. Long, R. K. Reed, and P. H. Klein, *Phys. Rev. B* **45** (1992) 9266.
- [43] E. Goering, PhD thesis, Universität Augsburg, 1996.
- [44] E. Goering, M. Schramme, O. Müller, H. Paulin, M. Klemm, M. L. denBoer, and S. Horn, *Physica B* **230-232** (1997) 996.
- [45] E. Goering, M. Schramme, O. Müller, R. Barth, H. Paulin, M. Klemm, M. L. denBoer, and S. Horn, *Phys. Rev. B* **55** (1997) 4225.
- [46] C. Blaauw, F. Leenhouts, F. van der Woude, and G. A. Sawatzky, *J. Phys. C* **8** (1975) 459.
- [47] M. Abbate, F. M. F. de Groot, J. C. Fuggle, Y. J. Ma, C. T. Chen, F. Sette, A. Fujimori, Y. Ueda, and K. Kosuge, *Phys. Rev. B* **43** (1991) 7263.
- [48] O. Müller, E. Goering, J. P. Urbach, T. Weber, H. Paulin, M. Klemm, M. L. denBoer, and S. Horn, *J. Phys. IV France* **7**, Colloque C2 (1997) 533.
- [49] P. F. Bongers, *Solid State Commun.* **3** (1965) 275.
- [50] K. Kosuge, *J. Phys. Soc. Jap.* **22** (1967) 551.
- [51] C. N. Berglund and H. J. Guggenheim, *Phys. Rev.* **185** (1969) 1022.
- [52] P. J. Brown, and K. R. A. Ziebeck, *J. Phys. C* **11** (1978) 2791.
- [53] T. Kawakubo, *J. Phys. Soc. Jap.* **20** (1965) 516.
- [54] C. J. Hearn, *J. Phys. C* **5** (1972) 1317.
- [55] E. Caruthers, L. Kleinman, and H. I. Zhang, *Phys. Rev. B* **7** (1973) 3753.
- [56] M. Gupta, A. J. Freeman, and D. E. Ellis, *Phys. Rev. B* **16** (1977) 3338.
- [57] A. V. Nikolaev, Y. N. Kostrubov, and B. V. Andreev, *Sov. Phys. Solid State* **34** (1992) 1514.
- [58] P. B. Allen, R. M. Wentzcovitch, W. W. Schulz, and P. C. Canfield, *Phys. Rev. B* **48** (1993) 4359.
- [59] E. Z. Kurmaev, V. M. Cherkashenko, Y. M. Yarmoshenko, S. Bartkowski, A. V. Postnikov, M. Neumann, L.-C. Duda, J. H. Guo, J. Nordgren, V. A. Perelyaev, and W. Reichelt, *J. Phys.: Cond. Matt.* **10** (1998) 4081.
- [60] E. Caruthers and L. Kleinman, *Phys. Rev. B* **7** (1973) 3760.
- [61] W.-D. Yang, PhD thesis, Universität Augsburg, 1999.
- [62] A. Continenza, S. Massidda, and M. Posternak, *Phys. Rev. B* **60** (1999) 15699.
- [63] W. H. Rosevear and W. Paul, *Phys. Rev. B* **7** (1973) 2109.
- [64] J. P. Pouget, H. Launois, T. M. Rice, P. Dernier, A. Gossard, G. Villeneuve, and P. Hagenmuller, *Phys. Rev. B* **10** (1974) 1801.
- [65] M. Ghedira, J. Chenavas, and M. Marezio, *J. Phys. C* **10** (1977) L309.
- [66] M. Ghedira, H. Vincent, M. Marezio, and J. C. Launay, *J. Solid State Chem.* **22** (1977) 423.
- [67] J. P. D'Haenens, D. Kaplan, and J. Tuchendler, *Solid State Commun.* **15** (1974) 635.
- [68] J. P. D'Haenens, D. Kaplan, and P. Merenda, *J. Phys. C* **8** (1975) 2267.
- [69] J. C. Bonner, M. E. Fischer, *Phys. Rev.* **135** (1964) A640.
- [70] J. P. Pouget, H. Launois, J. P. D'Haenens, P. Merenda, and T. M. Rice, *Phys. Rev. Lett.* **35** (1975) 873.
- [71] S. Westman, *Acta Chim. Scand.* **15** (1961) 217.
- [72] P. I. Sorantin and K. Schwarz, *Inorg. Chem.* **31** (1992) 567.
- [73] P. Hohenberg and W. Kohn, *Phys. Rev.* **136** (1964) B864.
- [74] W. Kohn and L. J. Sham, *Phys. Rev.* **140** (1965) A1133.
- [75] S. Matar, G. Demazeau, J. Sticht, V. Eyert, and J. Kübler, *J. Phys. I France* **2** (1992) 315; *J. Phys. I France* **4** (1994) 1259.
- [76] S. Matar, V. Eyert, J. Sticht, J. Kübler, and G. Demazeau, *J. Phys. I France* **4** (1994) 1199.
- [77] A. R. Williams, J. Kübler, and C. D. Gelatt, Jr., *Phys. Rev. B* **19** (1979) 6094.
- [78] V. Eyert, PhD thesis, Technische Hochschule Darmstadt, 1991.

- [79] J. Kübler and V. Eyert, *Electronic structure calculations*, in: *Electronic and Magnetic Properties of Metals and Ceramics*, edited by K. H. J. Buschow, VCH Verlagsgesellschaft, Weinheim 1992, pp. 1-145. Volume 3A of the series: *Materials Science and Technology*, edited by R. W. Cahn, P. Haasen, and E. J. Kramer, VCH Verlagsgesellschaft, Weinheim 1991-1996.
- [80] V. Eyert, *Basic notions and applications of the augmented spherical wave method*, Int. J. Quantum Chem. **77** (2000) 1007, special issue: *Electronic Structure of Materials*, edited by M. Defranceschi.
- [81] O. K. Andersen, Phys. Rev. B **12** (1975) 3060.
- [82] V. Eyert and K.-H. Höck, Phys. Rev. B **57** (1998) 12727.
- [83] V. Eyert, J. Comp. Phys. **124** (1996) 271.
- [84] R. Hoffmann, *Solids and Surfaces: A Chemist's View of Bonding in Extended Structures*, VCH, New York 1988.
- [85] V. Eyert and S. F. Matar, unpublished results.
- [86] V. Eyert, B. Siberchicot, and M. Verdaguer, Phys. Rev. B **56** (1997) 8959.
- [87] R. Dronskowski and P. E. Blöchl, J. Phys. Chem. **97** (1993) 8617.
- [88] N. Börnsen, B. Meyer, O. Grotheer, and M. Fähnle, J. Phys.: Cond. Matt. **11** (1999) L287.
- [89] N. Börnsen, G. Bester, B. Meyer, and M. Fähnle, J. Alloys Comp. **308** (2000) 1.
- [90] O. Müller, PhD thesis, Universität Augsburg, 1996.
- [91] J. J. Yeh and I. Lindau, At. Data Nucl. Data Tables **32** (1985) 1.
- [92] F. M. F. de Groot, M. Grioni, J. C. Fuggle, J. Ghijsen, G. A. Sawatzky, and H. Petersen, Phys. Rev. B **40** (1989) 5715.